Modeling the initial impact of storm events on the deformation and migration of full-grown sand waves

Thom Goesten

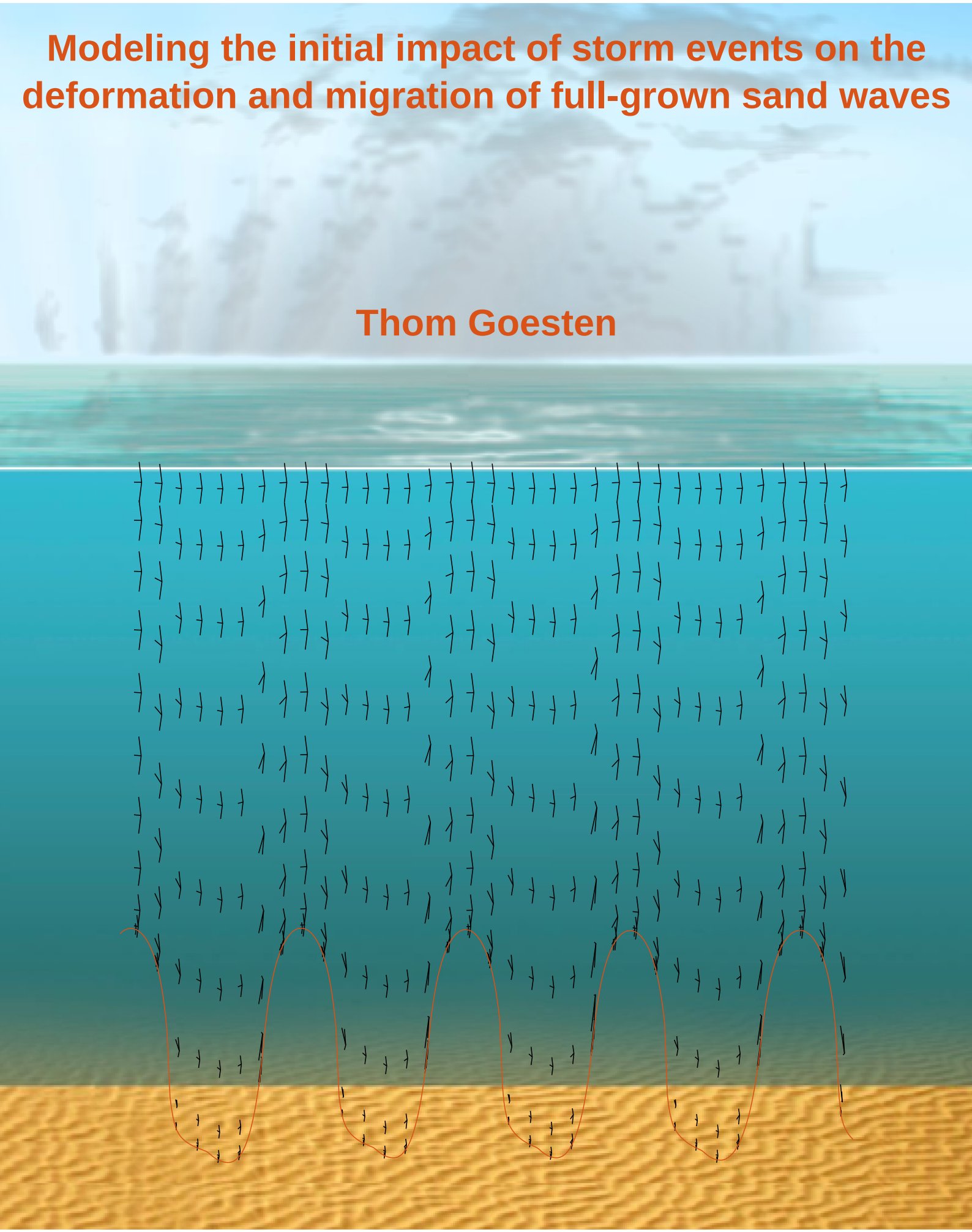

Front page figure adapted from Hoood (2017)

Modeling the initial impact of storm events on the deformation and migration of full-grown sand waves

a Delft3D modeling study

by:

Thom Goesten

To obtain the degree of:

Master of Science
at the University of Twente,
faculty of Engineering Technology,
study of Civil Engineering & Management,
research group of Marine & Fluvial Systems

to be presented on July 13^{th}, 2023

Author:
T.C.M. (Thom) Goesten s1989197

Graduation committee:
Dr. ir. B.W. (Bas) Borsje Committee chair
Dr. ir. J.H. (Johan) Damveld Daily supervisor
P.H.P. (Pauline) Overes MSc Daily supervisor

UNIVERSITY OF TWENTE.

Abstract

Sand waves are dynamic rhythmic bed patterns of several meters in height and are created by tidal circulation cells. They migrate over the continental shelf and thereby interfere with human interventions such as (energy) infrastructure. The hydrological and morphological effects during wind and surface wave action on the sand wave dynamics determine the extreme conditions and are therefore of interest for marine construction works. Therefore wind and surface wave action is implemented to a Delft3D model, which is based on van Gerwen et al. (2018), by allowing surface elevation and coupling to SWAN. Wind and surface wave conditions with a return value of 100 years are tested on full-grown sand waves. The results show that the inclusion of wind results in an ebb-directed bottom flow. Surface waves on the other hand increase flood-directed flows and increase turbulence, resulting in extra morphologic impact. The combination of wind and waves results in sediments migrating anti-wave-directed towards the previous sand wave slope. In total, the flattening of a sand wave during a once-in-a-100-years storm of 2.5 days is about as large as 20 years of tidal sand wave growth, making surface wave influences a crucial factor in modeling sand wave dynamics.

Highlights

- Sand wave steepness and height are reduced during storms.
- Surface waves result in much larger morphologic changes compared to wind-driven shear stress.
- During storms with large surface waves, sediments are transported anti-wave-directed, although sand waves migrate wave-directed.

Table of Contents

List of Symbols and Abbreviations

Mathematical symbols

Symbol	*Description*	*Unit*
C_d	drag coefficient	-
d	average depth bathymetry	m
g	acceleration due to gravity	ms^{-2}
H	height water column	m
H_s	significant height of surface waves	m
I	Storm intensity	-
k	turbulent kinetic energy	$\mathrm{m}^2\mathrm{s}^{-2}$
R	Riemann invariant	ms^{-1}
t	time	s
T_s	significant wave period	s
u	velocity in x-direction	ms^{-1}
U	depth-averaged horizontal velocity	ms^{-1}
U_{10}	wind speed 10 m above surface	ms^{-1}
x	horizontal coordinate	m
z	vertical coordinate	m
z_b	bed level	m
ϕ	sand wave slope	$^\circ$
λ	sand wave wavelength	m
σ	vertical direction	-
ω	velocity in σ-direction	ms^{-1}
ω_w	angular wave frequency	s^{-1}
θ	wave direction	$^\circ$
ζ	surface elevation	m
$\langle\cdot\rangle$	tide averaged	
$\vec{\cdot}$	directed value	
$\bar{\cdot}$	magnitude	

Abbreviations

Abbr.	*Description*
2DH	2 Dimensional horizontal
2DV	2 Dimensional vertical
FGM	Fastest growing mode
M2	semi-diurnal lunar constituent
M4	quarter-diurnal lunar constituent
TKE	turbulent kinetic energy

1 Introduction

Tidal forces in shallow seas affect, under favorable conditions, the sandy bed, resulting in dynamic rhythmic bed patterns (Dijk and Kleinhans, 2005). One of the dominant patterns are sand waves, which are several meters high and hundreds of meters long (Besio et al., 2006). The rhythmic patterns are constantly affected by tidal forcing, however short-term processes, such as wind and surface waves, are expected to play a crucial role as well in the migration, the deformation, and the growth of the sand waves (Besio et al., 2006; Campmans et al., 2018b). Storms affect sediment transport by for example increasing the turbulence in the water column, creating a pressure-driven flow, and increasing orbital velocities (Gargett and Savidge, 2020). In general, these processes increase the bed velocity and result in increased sediment transport and hence morphological change.

The continental shelf of the North Sea is actively utilized in the past decades, mainly for offshore (energy) harvesting, pipeline infrastructure, navigation, and for coastal protection. In the upcoming years, it is expected that these activities will increase (Vrees, 2021). A better understanding of the sub-aqueous forces and their possible impact on human interventions is essential for better utilization of the North Sea area. Moreover, highly energetic storm events create large hydro- and morphodynamic forces and determine the limits of marine engineering. The influence of storms moreover is expected to grow, as storms are expected to become more frequent and have larger intensities, due to climate change. Knowledge about the storm effects on sand waves is therefore crucial to make the energy transition towards sustainable energy and to create nature-based solutions for climate change (Kumar et al., 2021).

Tidal flows over a disturbed bed result in residual vertical circulation cells that enhance sand wave growth (Hulscher, 1996). Tidal asymmetry or other net-directed forces result in a sand wave asymmetry (Besio et al., 2003) and migration of sand waves (Knaapen, 2005). Sediment transport is dependent on the bottom flow velocity, turbulence, and sediment characteristics. When the bed shear stress overcomes the critical bed shear stress, sediments will be transported, either a bed load or suspended load. In general, bed load transport is dominant and responsible for continuous growth and migration (Naqshband et al., 2014), while suspended sediment transport increases turbulence and reduces sand wave growth (Tonnon et al., 2007).

Storms have an impact on this process in two ways, by the influence of wind action and surface wave action (Liang et al., 2022). Wind action is the shear stress on the water surface, resulting in dominant flow patterns. Asymmetric flow profiles result in a dominant migration direction. Moreover, the shear stress enhances surface wave formation and growth (Lee and Monty, 2020). Surface waves create orbital motions in the water, propagate along the surface, and affect the layers below. This orbital motion results in a wave-directed mass drift, which is called Stokes drift (Bremer and Breivik, 2018). Surface waves enhance turbulence (Babanin, 2006) and therefore bed shear stress and sediment transport (Damen et al., 2018; Sumner, 2023).

Measurement studies have already shown that highly energetic storm events influence the morphology in the long term (Fenster et al., 1990; Passchier and Kleinhans, 2005). In the short term, Bao et al. (2020) showed that one tropical storm (wind speeds of 21 ms^{-1}) results in a sand wave decrease of 1.2 m in the Taiwan Shoal, which is not expected to recover in one year. Moreover, both shoals have similar depths, although in the Taiwan Shoal sand waves, in general, are larger (15 m) compared to the North Sea (7 m). However, pre- and post-storm measurements do not show the effects of sediment transport and concentrations during a storm. Instead, process-based models on sand wave dynamics can give insight (Borsje et al., 2013). Van Gerwen et al. (2018) determined the growth and migration rates of initial-stage sand waves up to full-grown sand waves. The results show realistic growth rates although the height of sand waves in general is overestimated and migration rates were underestimated (Wang et al., 2019). This can possibly be explained by the exclusion of wind-wave interactions.

Liang et al. (2022) continued on these models and tested moderate wind and wave conditions on initial sand waves, which indeed showed reduced growth rates. Hereby the interaction of 4 processes was added; (i) wave-induced drift, (ii) additional shear stress at the water surface,

(iii) wave-induced turbulence, and (iv) enhanced bed shear stresses. Moreover, the model shows migrating sand waves opposed to the wave propagation direction, which are enhanced by increased suspended sediment concentrations in combination with a return flow due to Stokes drift. A linear model study of Campmans et al. (2017) showed that wind and surface waves reduce growth rates and increase migration rates of sand waves. The nonlinear study (Campmans et al., 2018b), shows that a dynamic sand wave equilibrium results from intermittent storms, with lower sand waves.

In reality, sand waves are also continuously in a quasi-equilibrium, and adapt to the hydrodynamic conditions. In this study, the goal is to describe how this quasi-equilibrium is affected during extreme storms, hydrologically and morphologically and how sediment volumes are transported. A process-based modeling study, focusing on the short-term effects of extreme weather conditions, that determines the limits for marine engineering, is therefore of interest. The goal of the thesis therefore is,

---

to determine the initial impact of storm events on the deformation and migration of full-grown sand waves.

In order to answer this question, first the Delft3D model and its assumptions are explained (Chapter 2) and extra focus is given to the adaptations made compared to the model of van Gerwen et al. (2018) in Chapter 3. Next, the results will be discussed, in Chapter 4 the hydrodynamical effects of wind and surface waves in a sand wave system are analyzed and Chapter 5 focuses on the morphodynamics effects. Finally, the results are put in perspective in the Discussion (Chapter 6) in order to give the conclusions on Page 19.

2 Model description

The simulations are done in a process-based numerical model, Delft3D 4 (Deltares, 2023a), which is able to simulate unsteady flow and transport phenomena in, among others, shallow seas. It consists of several modules, with as basis the Delft3D-Flow module. In every simulation step, the Delft3D-Flow module solves the Navier-Stokes equations assuming incompressible fluids in shallow water and hydrostatic pressure under Boussinesq assumptions to determine the flow field (Deltares, 2023a). In this study, the model is used in 2DV-mode, only considering variations in x- and z-direction. The grid is a rectangular staggered grid, meaning that the velocities are calculated on the edges of all cells, while the surface elevation and densities are calculated at the center of each cell. Moreover, in each cell, it is assumed that all other parameters (i.e. depth, sediment concentration, bed slope) are constant. In the z-direction, a σ-grid is applied, in which the layers are defined by the relative height and thus dependent on the water depth. As a result, the continuity and momentum equations are reduced to,

$$\frac{\partial \zeta}{\partial t} + \frac{\partial (Hu)}{\partial x} = Q, \tag{1}$$

hereby ζ is the surface elevation [m] in time t [s], H is the water depth [m] and u is the water velocity [ms^{-1}] in horizontal direction x [m]. Q [$\mathrm{m^2 s^{-1}}$] represents the net discharge of water. The vertical velocities are computed from the continuity equation, while the horizontal velocities are based on the momentum equation,

$$\frac{\partial u}{\partial t} + u\frac{\partial u}{\partial x} + \frac{\omega}{H}\frac{\partial u}{\partial \sigma} = F_P + F_R + F_v + F_e + F_w, \tag{2}$$

where ω is the velocity [$\mathrm{ms^{-1}}$] in σ-direction [-] and F_P, F_R, F_v, F_e, and F_w represent the forces acting on the water body based on the pressure gradient [$\mathrm{m\ s^{-2}}$], Reynolds stresses, viscosity, external sources, and waves respectively. The wave force is calculated using the radiation stress (S [$\mathrm{m^2\ s^{-2}}$]) along; $F_w = -\frac{\partial S}{\partial x}$.

The wind is included as shear stress on the water surface in the Delft3D-Flow module. This shear stress is included as a boundary condition for the momentum equation on the water surface,

$$\left.\frac{\nu_v}{H}\frac{\partial u}{\partial \sigma}\right|_{\sigma=0} = \frac{|\tau_s|}{\rho_0}. \tag{3}$$

where ν_v is the vertical eddy viscosity [$\mathrm{m^2 s^{-1}}$], ρ_0 is the water density [$\mathrm{kg\ m^{-3}}$], and τ_s is the shear stress [$\mathrm{kg\ m^{-1}\ s^{-2}}$], which is defined as $|\tau_s| = \rho_a C_d U_{10}^2$, where C_d is the wind drag coefficient [-], ρ_a is air density ($\rho_a = 1\ \mathrm{kg\ m^{-3}}$), and U_{10} is the wind velocity [$\mathrm{ms^{-1}}$] at 10 m above the surface.

The Delft3D-Flow module is coupled to the Delft3D-Wave module, which is a third-generation SWAN model (Deltares, 2023b), and makes use of a 2DH-grid. Every time the module is activated, the wave action density spectrum is determined. This is based on the hydrodynamic input from the flow module, the wave characteristics at the boundaries, the wind-driven wave generation, dissipation, and non-linear wave-wave interactions, calculated using quadruplet wave-wave interaction according to Hasselmann et al. (1985). Moreover, the wave generation by wind is implemented as a combined linear and exponential growth term. Dissipation based on whitecapping, bottom friction, and depth-induced breaking are implemented and individually calculated. The whitecapping is calculated using the method of Komen et al. (1984). The bottom friction dissipation is calculated using the Jonswap method and dissipation due to wave breaking is modeled dependent on the water depth.

In the Flow-module, the surface waves result in Stokes drift, streaming, enhanced bed shear stresses, and increased turbulence. The enhanced velocities due to Stokes drift (u^s [$\mathrm{ms^{-1}}$]) are calculated in the Flow module according to,

$$u^s(z) = \frac{\omega_w k H_s^2 cosh(2kz)}{2 sinh^2(kH)}, \tag{4}$$

where ω_w is the angular frequency of waves [s^{-1}], k is the turbulent kinetic energy [m^2 s^{-2}], defined by its own transport equation, H_s is the significant surface wave height [m], z is the depth [m] of the total height of the water column (H [m]). Streaming also results in a wave-induced current, however in the bottom region (for z in the boundary layer δ [m]), as is given by:

$$\frac{\partial u}{\partial z} = \frac{D_f k cos(\phi)}{\rho_0 \omega_w \delta} \left(1 - \frac{H - z}{\delta}\right) \tag{5}$$

where D_f is the dissipation due to frictionand ρ_0 is the water density ($\rho_0 = 1 \cdot 10^3$ kg m^{-3}).

The enhanced bed shear stress due to surface waves (τ_w [kg m^{-1} s^{-2}]) is modeled as,

$$|\vec{\tau_w}| = \frac{1}{2}\rho_0 f_w u_{orb}^2, \tag{6}$$

where f_w is the friction coefficient [-] and u_{orb} is the orbital velocity [ms$^-$1] computed from linear wave theory, along $u_{orb} = \frac{1}{4}\sqrt{\pi}\frac{H_{rms}\omega_w}{sinh(kH)}$, where H_{rms} is the root mean square of the surface wave height [m]. The mean bed shear stress (τ_m [kg m^{-1} s^{-2}]) is corrected for the Stokes drift by using:

$$\vec{\tau}| = \frac{\langle \tau_m \rangle}{\langle u \rangle}\vec{u} - \vec{u}^s, \tag{7}$$

Last but not least, wind and surface waves also affect turbulence. The turbulence is computed according to the $k - \epsilon$ turbulence model. This model assumes shallow water and is based on two transport equations instead of the conservation of turbulent quantities. One of the transport equations is based on the turbulent kinetic energy (k [m^2 s^{-2}]) and the other is based on energy dissipation (ϵ [m^2 s^{-3}]). The influence of wind and waves on the turbulence is modeled using a boundary condition at the top surface,

$$k|_{\sigma=0} = \frac{u_{*s}^2}{\sqrt{c_\mu}} + \left(\frac{2D_w\kappa}{\rho_0 c_D}\right), \tag{8}$$

$$\epsilon|_{\sigma=0} = \frac{u_{*s}^3}{\frac{1}{2}\kappa\Delta z_s} + \frac{4D_w}{\rho_\omega H_s}. \tag{9}$$

In both equations, the first term represents the wind enhancement and the second term represents the influence of surface waves. u_{*s} is the friction velocities at the surface [m s^{-1}], Δz_s is the change in surface elevation, κ is the von Karman constant ($\kappa = 0.41$ [-]), H_s is the significant surface wave height [m], D_w is the turbulent energy generation due to wave breaking [W m^{-2}], c_μ is an empirical constant ($c_\mu = 0.09$ [-]), and c_D is the drag coefficient [-].

The results of SWAN are communicated to Delft3D-Flow interactively, resulting in two-way wave-current interactions. In the Delft3D-Flow module, the results of Delft3D-Wave are implemented in a wave-averaged manner. The surface waves do therefore not show surface elevation or temporal velocity change.

Sediment transport is calculated using the transport equation of Rijn (1993) based on near-bed velocities. In this method, bed load transport rate (S_b [kg m^{-1} s^{-1}]) and suspended load transport rate (S_s [kg m^{-1} s^{-1}]) are calculated separately, namely along;

$$|S_b| = 0.006\rho_s\omega_s D_{50} M^{0.5} M_e^{0.7} \tag{10}$$

$$S_s = f_{susw}\gamma U_A L_T \tag{11}$$

where the full explanation of all variables is given in Appendix A, but the bed load is mainly dependent on the sediment diameter (D_{50} [m]) and mobility numbers (M [-]), while the suspended load is on the velocity asymmetry (U_A [ms^{-1}]) and the suspended load (L_T [kg m^{-2}]).

3 Method

The model presented in this paper is based on the numerical models constructed by Borsje et al. (2013) and van Gerwen et al. (2018), and adjusted for modeling wind and wave conditions. In this chapter an overview of the model adaptations and model cases (as can be seen in Table 1) is given, and extra information can be found in Appendix B.

3.1 Model setup

The grid of the model consists of 2 m wide horizontal cells in the area of interest, in which one central sand wave (see green box in Figure 1) is surrounded by 1.5 wavelengths of fully sized sand waves on both sides (2 crests and 1 trough). Next to that on each side, 1.5 wavelengths of decreasing sand waves (1 crest, 2 troughs) are used as a connection to the flat domain. Towards the boundaries, the cells grow up to 1500 m in length, and the total grid is 20 km long. In the vertical direction, the σ-grid is refined at the top and bottom surface, resulting in 60 vertical layers. The top and bottom layers consist of 0.05% of the depth and the center cells span 2.75% of the depth. The grid is visualized in Figure 1.

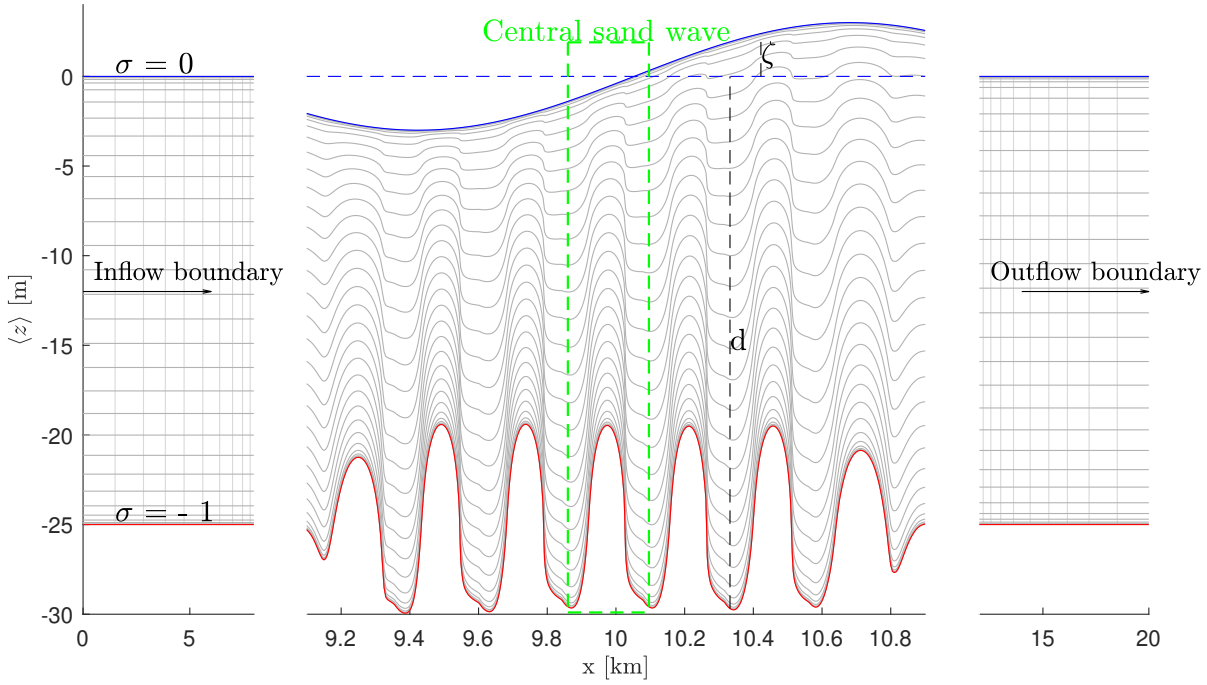

Figure 1: Illustration of the domain.
For demonstrative purposes, the tidal frequency is increased and only given in the area of interest, in which the horizontal grid is not visualized. Moreover only half of the depth layers are shown. *Note the different horizontal axes.*

The tidal forcing is constrained on the two open boundaries, parallel to the sand waves' crests, using Riemann invariants. The Riemann invariant results in a weakly reflective boundary, meaning that waves are able to propagate out of the domain. The tidal forcing is applied to the inflow boundary, at the outflow boundary a Riemann invariant of 0 ms^{-1} ensures an almost undisturbed outflow of the tide. This results in a spatially and temporally propagating tidal wave, as can be seen in Figure B.1. The flood originates from the left (inflow boundary), while the ebb flow is opposed. The astronomic force applied in the model is the M2 (the semi-diurnal lunar constituent) and its higher harmonic M4. Together an asymmetric tide is created while preserving the M2 frequency. A ratio of 18:1 is representable for the M2 and M4 amplitudes (Gräwe et al., 2014) with a phase shift of 40°(Overes, 2021). In model studies, the velocity amplitude of 0.65

ms^{-1} is often used as the M2-value for the North Sea conditions (Borsje et al., 2013; Werf et al., 2022). Measurements show corresponding mean surface elevations of about 0.8 to 1.5 m (Pedersen et al., 2008; Reynaud and Dalrymple, 2012; Jänicke et al., 2021). Implementing this to the user input of the Riemann invariant ($f(t)$ [ms^{-1}]) of Delft3D,

$$f(t) = U(t) \pm \zeta(t)\sqrt{\frac{g}{d}}, \tag{12}$$

results in a $f(t)$ of 1.15 to 1.59 ms^{-1}. Where $U(t)$ is the depth-averaged tidal velocity amplitude [ms^{-1}], ζ is the surface elevation amplitude [m], d is the tide-averaged depth [m], and g is the gravitational acceleration [ms^{-2}]. When ranging over these Riemann values, in combination with a Chézy value of 75 and an α_{bs} of 3, it is found that a R_{M2} = 1.30 ms^{-1}, combined with R_{M4} = 0.072 ms^{-1} with a phase lag of $\phi_{M4} = 40°$, results in realistic velocity amplitudes around 0.65 ms^{-1}.

The dominant sand wave wavelength is determined by a fastest growing mode analysis (FGM), in which the sand wave wavelength is determined by finding the largest growth rate for initial sand waves (Hulscher et al., 1993). Using the dominant mode, (λ = 232 m), the equilibrium bathymetry is determined based on a long-term run with only tidal forcing. This equilibrium bathymetry is asymmetric, as can be seen in Figure 1 with steeper slopes on the ebb slide (right) compared to the flood side (left) of each sand wave. Moreover, the sand waves show flood-directed migration caused by the combination of tidal constituents (Besio et al., 2003). The sand waves are about 10.2 m high, which is larger compared to observations (Damen et al., 2018) and can possibly be explained by the absence of wind and wave effects. More information about the establishment of the equilibrium bathymetry can be found in Appendix B.2.

At the input boundaries of the SWAN module, the wave height and wave period are manually constrained. The ratio between the significant wave height (H_s [m]) and wave period (T_s [s]) is dependent on the wind-driven wave growth, based on time and fetch. It is chosen to define the boundary conditions according to the equations of Carter (1982), in which the wave growth is limited by fetch (X [m]),

$$\begin{aligned} H_s &= 0.0163 X^{0.5} U_{10} \\ T_s &= 0.439 X^{0.3} U_{10}^{0.4} \end{aligned} \tag{13}$$

In order to model the large wind shear stresses on the water surface accurately, the drag coefficient (C_d) has been adjusted according to Makin (2005),

$$C_d = \begin{cases} 0.05 U_{10} + 0.90, & \text{for } U_{10} <= 30.8 \text{ ms}^{-1}, \\ -0.0333 U_{10} + 3.4667, & \text{for } U_{10} >= 30.8 \text{ ms}^{-1}, \end{cases} \tag{14}$$

where U_{10} the wind speed 10 m above sea level is.

3.2 Model cases

In this research, 4 cases are defined (Reference, Wind, Waves, and Wind and waves). The Reference case only consists of tide and is used to determine the equilibrium bathymetry. In the other 3 cases, once-in-a-100-year storm conditions are implemented, approaching from the flood direction. In Table 1, an overview is given of the model and case parameters.

Every run starts with a spin-up of one tidal cycle, in which the velocity field, turbulence, and suspended sediment concentrations are able to settle, but no bathymetry updating is present yet. After that, 5 full tidal cycles, starting with flood and ending with ebb are simulated including morphologic change. The SWAN model is connected and updates the wave field every communication timestep (t_s [s]). In the Reference and Wind case, no surface waves are generated. In the other cases, surface waves are created and the hydrodynamical conditions in the Flow module are adapted subsequently. Wind-driven wave growth and quadruplet wave-wave interactions are only

activated in the combined Wind and wave case, as these non-linear processes are a result of wind and wave interactions. As a result, surface waves in the area of interest are larger in the Wind and wave case compared to the Wave-case, and can therefore not be compared directly. Moreover, the surface waves are not spatially constant.

At the end of every run, data is loaded to Matlab, to be processed. In general, the results around the central sand wave are used for analysis and are quantitatively compared to the two neighboring sand waves to ensure good agreement. The morphologic change is based on the spline interpolated central sand wave. In spline interpolation, low-degree polynomials are used to determine values in between the grid cells. The height is calculated as the height difference between the top and the mean of both troughs. The migration is determined based on the displacement of the spline interpolated top, and deformation is quantitatively analyzed and qualitatively based on both slopes, measuring the mean slope from 20% to 80% of the sand wave height.

Table 1: Overview of model parameters and scenarios

Description	*Symbol*	*Value*		*Unit*
Chézy roughness	C	75		$\mathrm{m}^{\frac{1}{2}}\mathrm{s}^{-1}$
Tide-averaged water depth	d	25		m
Bed slope correction factor	α_{bs}	3.0		-
Simulation timestep	δ_t	6.0		s
Morphological acceleration factor	MF	1		-
Median grain size	D_{50}	350		μm
Tidal amplitude of M2	R_{M2}	1.3		ms^{-1}
Tidal period of M2	T_{M2}	12.42		h
Tidal amplitude of M4	R_{M4}	7.2	$\cdot 10^{-2}$	ms^{-1}
Tidal period of M2	T_{M2}	6.21		h
Tidal shift M4 w.r.t. M2	ϕ_{M4}	40		°
Wind direction	θ_{wind}	270		°
Surface wave propagation direction	θ_{wave}	270		°
Background diffusivity	D_H^{back}	0.2		$\mathrm{m}^2\mathrm{s}^{-1}$
Background viscosity	ν_H^{back}	0.2		$\mathrm{m}^2\mathrm{s}^{-1}$
Simulation duration	θ_{wave}	82.57		h
Simulation timestep Delft3D-Flow	Δt_f	6		s
Simulation timestep Delft3D-Wave	Δt_w	9936		s

Model conditions		*Ref.*	*Wind*	*Waves*	*Wind & waves*	
Wind speed (10 m above surface)	U_{10}	0	32	0	32	ms^{-1}
Significant wave height	H_s	0	0	8.2	8.2	m
Significant wave period	T_s	-	-	9.2	9.2	s

The 100-year return values for the North Sea are wave heights of about 8.2 meters (Caires et al., 2006), and wind speeds (U_{10}) of about 32 m/s (Sterl et al., 2015). For the flood direction, a fetch of 250 km is estimated and used in the equations of Carter (1982). The impact of the storm intensity (I [-]) moreover is analyzed for the Wind and Wave-case in section 5.3. Thereby the surface wave conditions are again based on the equations of Carter (1982) with a fetch of 250 km, while the wind conditions are determined along,

$$U_{10} = I \cdot U_{10max} \tag{15}$$

for a range of intensities of 0 to 1 [-]. Hereby the intensity of 0 is equal to the Reference case and U_{10max} is equal to the once-in-a-100-year wind speed.

4 Hydrodynamic results

In this chapter the hydrodynamic results of the 4 cases, as defined in Table 1, are discussed. Based on morphostatic runs, the velocity fields around the central sand wave are analyzed for each case. Next, the turbulent kinetic energy (TKE) spectra for all cases are analyzed based on the first tidal period of morphodynamic runs.

4.1 Velocity field

First, the hydrodynamics of the reference case is analyzed, using its velocity field around the central sand wave (Figure 2a). It shows that the largest tide-averaged velocity magnitudes (color plot) are found above the crest of the sand wave, while the maximal tide-averaged directed velocity is found at the bed (vector plot). Moreover, the largest velocities can be seen at the surface and decrease towards the bottom, as can also be seen in velocity profiles (red line in Figure 4). On both sides of the sand wave, in Figure 2a, a circulation cell can be identified, resulting in a crest-directed flow on both sides of the sand wave, with the largest tide-averaged directed velocities at the steepest locations of the sand wave. The stagnation point, with no net velocities, is at the crest (red star in Figure 2a). In general, the plot shows a slightly ebb-directed flow, caused by larger velocities during ebb compared to flood, based on surface level decrease during ebb.

(a) Reference

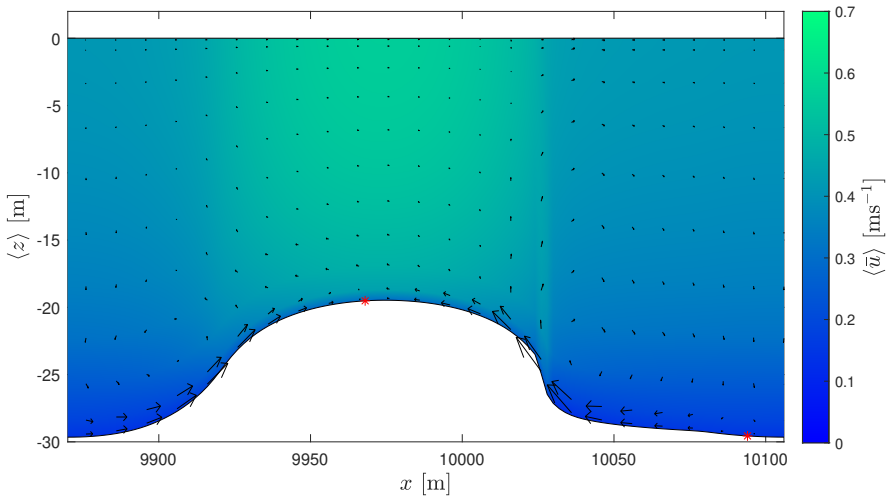

Figure 2: The absolute tide-averaged velocity magnitudes around the central sand wave (color plot) during a morphostatic run for each case. The arrows represent the directed tidal residual velocity over one tidal cycle and the red star represents the stagnation point(s).
Note: The figure continues on the next page with the other cases.

The addition of wind results in shear stress on the surface layer and therefore also increased wind-directed velocities in the top layers, as can be seen in the velocity field (Figure 2b) and the velocity profile (Figure 4). During a flood, the entire velocity profile is flood-directed, and the horizontal velocities in the top layers are enlarged due to the wind stress, with the largest velocities at the surface. However, during an ebb, the wind-driven shear stress only influences the top layers, while the tidal discharge is compressed to the layers below, resulting in large ebb-directed velocities at the bottom. This results in tide-averaged ebb-directed bottom velocities. Next to that, the wind-driven shear stress induces a constant wind-directed mass drift at the top layers, resulting in a set-up in the model. The setup is 0.19 m over the 20 km domain for windspeeds (U_{10}) of 32 ms^{-1} and enhances a return flow at the bottom in the order of 0.4 ms^{-1}. The tide-averaged velocity profile can be seen in Figure 4 and shows large wind-directed top velocities in combination with opposed bottom velocities. Moreover, in the velocity field (Figure 2b), the stagnation point has

(b) Wind

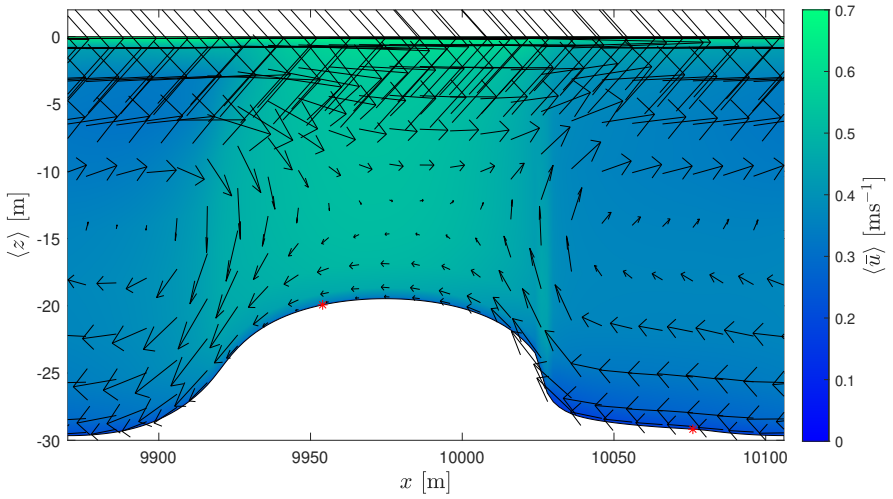

(c) Waves

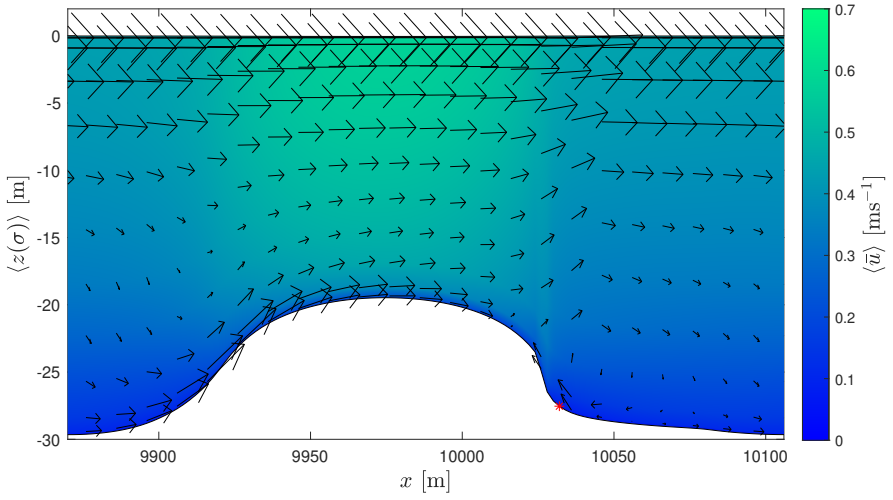

(d) Wind and waves

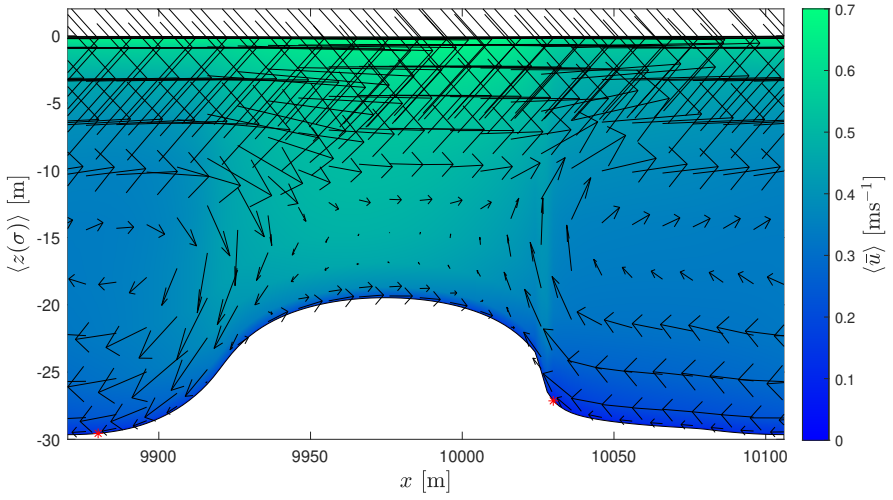

also shifted in the anti-wind direction, due to anti-wind-directed bottom velocities.

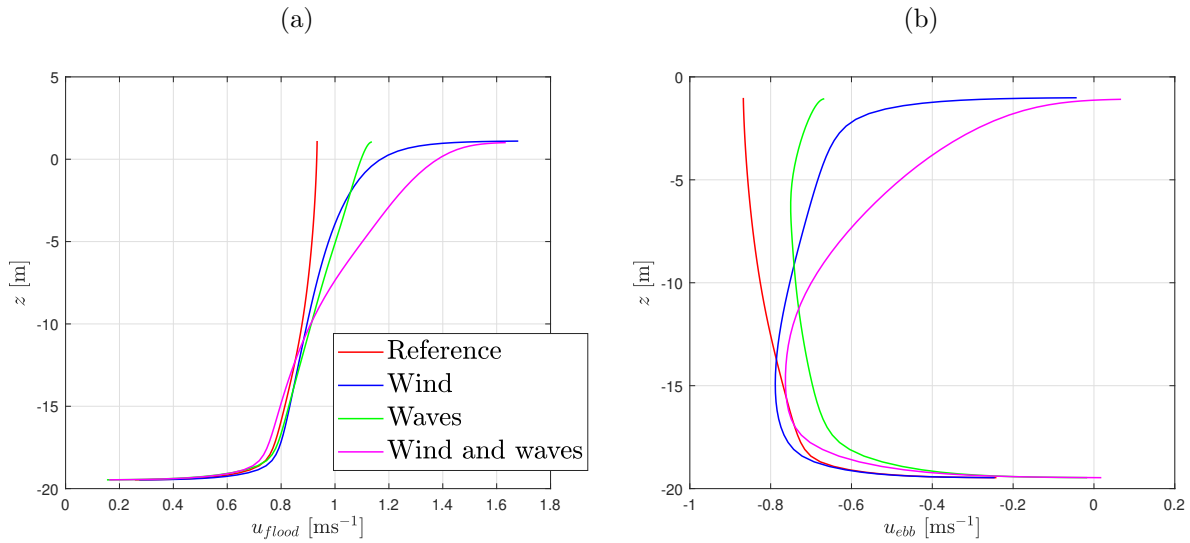

Figure 4: The depth velocity profile during the peak flow of (a) flood and (b) ebb at the top of the central sand wave

The inclusion of surface waves results in orbital motions around the surface layer in the Wave module. As a result, Stokes' drift, increased turbulence, enhanced bed shear stresses, and shearing are included in the Flow module. The Stokes drift at the top layers and the streaming at the bottom result in a wave-directed velocity field (Figure 2c) and due to the limited depth, the entire tide-averaged velocity profile in the Flow module is flood-directed (green line in Figure 5a). In this figure, the directed tide-averaged velocity decreases over the depth, according to the Lagrangian profile. However, the velocity profile close to the bottom again increases, as the tidal flow during ebb is more affected by the bottom friction, compared to the flood-directed flow during flood. The stagnation point has shifted in flood direction due to increased flood-directed bed velocities. For wave heights up to 6.2 m, the stagnation point stays on the crest (although shifted). For larger waves, the stagnation point has moved beyond the steep slope of the sand wave and circulation cells are not present anymore, as can be seen in Figure 2c.

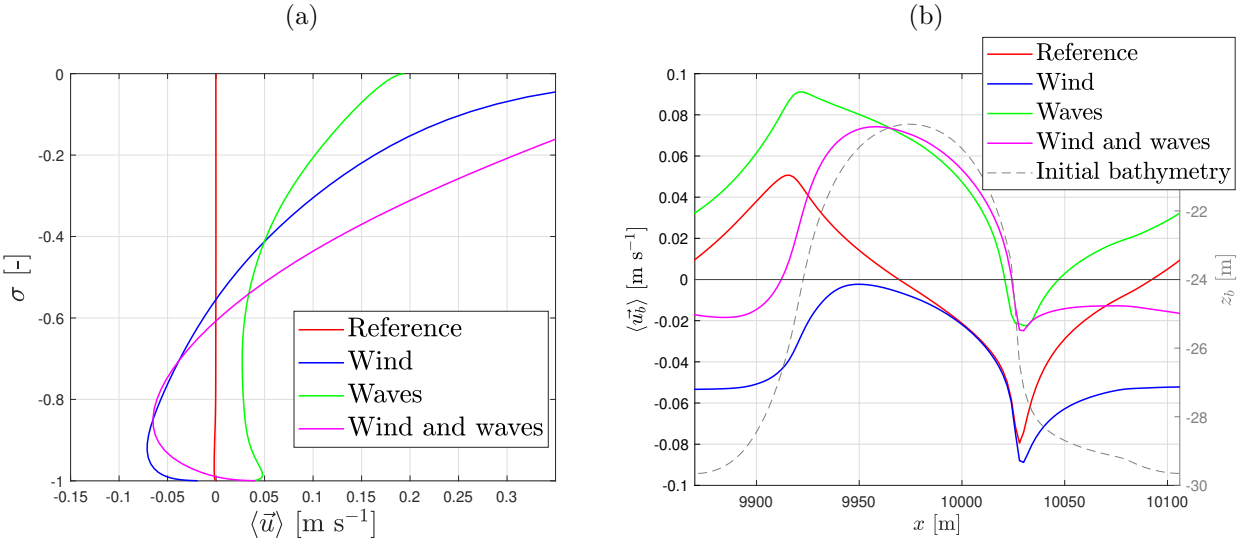

Figure 5: The tide-averaged velocities on the morphostatic central sand wave, showing a) the tide-averaged depth velocity profile and b) the spatial distribution of the directed tide-averaged bottom velocities. The bottom velocity is the weighted average of the bottom 6 layers, in total 0.8% of the depth.

The interaction between wind and surface waves results in wind-driven surface wave growth, resulting in larger surface waves. The velocity field is predominantly affected by the surface waves. However, the tide-averaged velocity field is predominantly affected by the wind and its return flow, as can be seen in Figure 2d. During flood, large velocities at the top layers are found, which decrease towards the bottom. During ebb, the wind shear on the surface and the wave propagation are opposed to the main flow direction, resulting in top velocities in the direction of the wind and surface waves, while velocities just below the surface are ebb-directed. Tide-averaged, the dominant velocity in the top half is flood directed, however in the bottom half, ebb-directed velocities are dominant, as can be seen in the pink line in Figure 4b. At the crest, flood-directed bottom velocities are dominant due to the wave action, while in the trough the ebb-directed velocities caused by wind action are dominant (Figure 5). The tide-averaged velocity field shows one large circulation cell in the trough (Figure 2d).

4.2 Turbulence

The sediment transport equations are mainly dependent on the local bottom velocities and therefore turbulent kinetic energy (k or TKE) is an important parameter for sediment transport (Tanaka et al., 2009) and changes over time, period, and by the presence of wind and surface waves. Therefore, the TKE is analyzed and for each case. The ride-averaged depth-TKE-profile is shown in the semilogarithmic Figure 6a, while Figure 6b shows the spatial distribution.

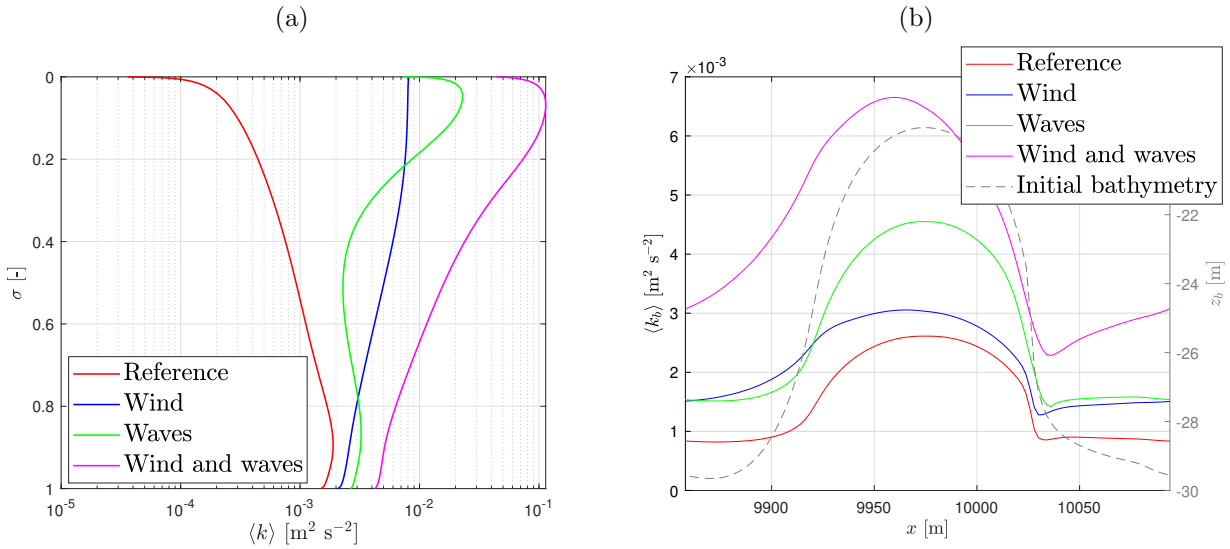

Figure 6: The tide-averaged turbulence kinetic energy (k) profile during the first tidal cycle of a morphodynamic bed in the central 3 sand waves, showing a) the variation per σ-layer on a semilog scale and b) the spatial variation at the 6 bottom layers (total 0.8% of the depth).

In the Reference case, the TKE is limited, but largest close to the bed and increases during ebb and flood. The combination of wind and/or surface waves with the tide, however, largely increases the TKE, especially at the top layers. For tide and wind, the largest turbulence is at the top (see dark blue in Figure 6a), where also the largest shear stresses are present. The TKE mainly increases when opposed flows, encounter each other. This is during an ebb at the top half of the water column and for a flood at the bottom.In the Wave-case, the largest tide-averaged TKE can be found at about 2 to 10% of the depth below the surface, as can be seen in the green line in Figure 6a. Here, also the largest vertical mixing processes are present. The bottom TKE (Figure 6b) is mainly increased at the crest due to the limited depth. The combination of wind and surface waves results in much larger TKE-values, this is partly caused by larger surface waves, but partly also by the nonlinear wind-wave interactions. Comparing the tide-averaged TKE at the bottom layers (Figure 6b), it can be seen that the largest tide-averaged TKE-values are found at the crests. However, the difference between the 4 scenarios is larger compared to the spatial differences.

5 Morphodynamic results

This chapter shows the morphodynamic results of the 4 cases, as are described in Table 1. The sediment transport and the field of sediment concentrations are analyzed based on the first tidal cycle. The morphologic change is analyzed based on the total simulation, consisting of 5 morphodynamical tidal cycles (about 2.5 days).

5.1 Sediment transport

Sediment in the reference case is affected by the tidal velocities. During peak tidal flows, the shear stress at the crest is large enough to overcome the critical bed shear stress, and sediments are thus transported. At the trough, sediments are only transported during flood peak flow. At the steep slope, the ebb-velocities are dominant (red line in Figure 5b), however, due to the large bed slope the sediment transport is opposed. In total, the tide-averaged sediment transport is flood-directed over the entire domain. The tide-averaged bed load and suspended load sediment transport are in the same order of magnitude as can be seen in Figure 7a, although they are not equally spatially distributed. Bed load on the sand wave is flood-directed and its magnitude is almost uniform over the sand wave crest, the suspended load is larger at the mild slope and even slightly negative at the steep slope. The suspended sediment concentrations are the largest at the crest and absent in the through, as can be seen in Figure 8.

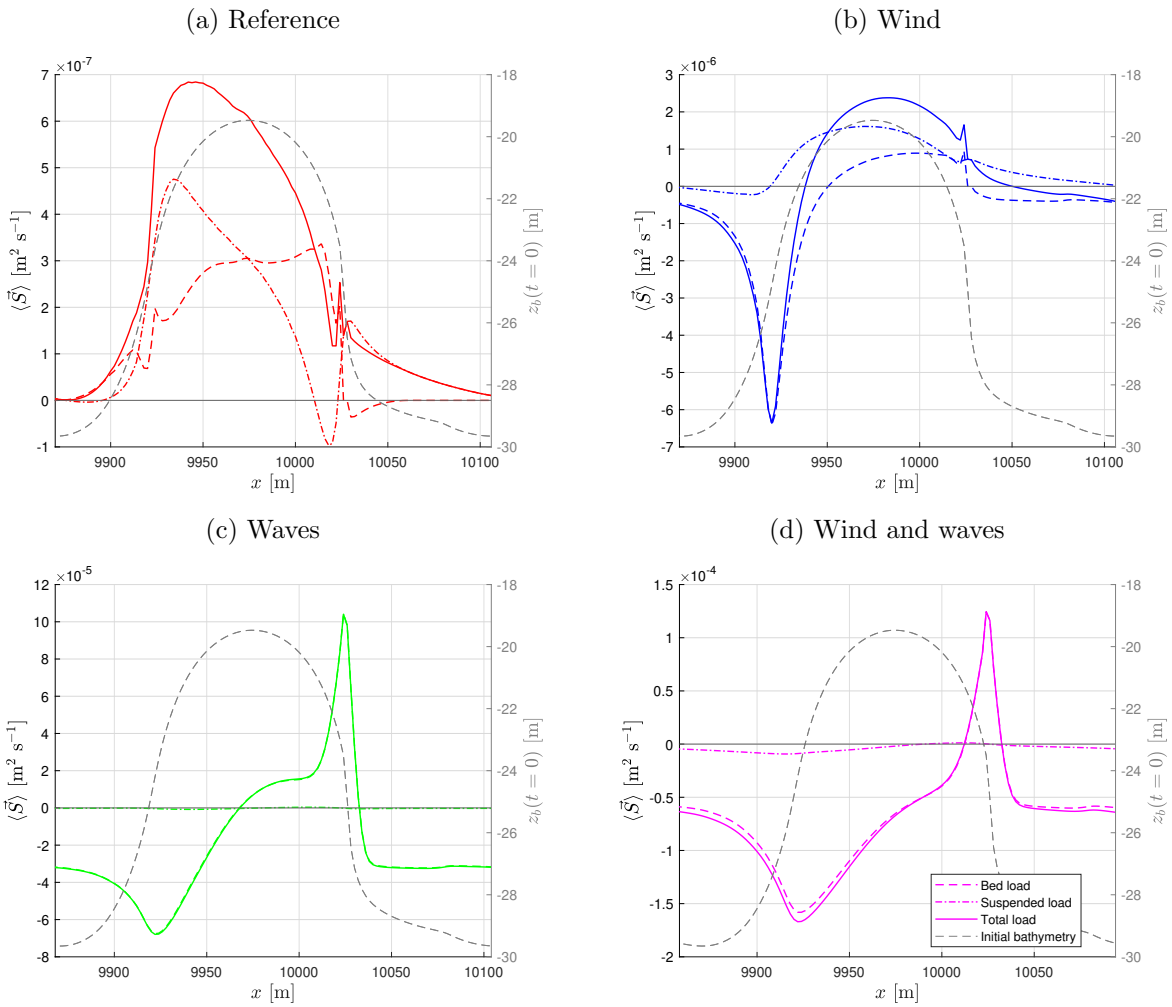

Figure 7: The spatial distribution of sediment transport volumes in x-direction for bed load (dashed), suspended load (dashdotted) and combined (solid) during the first full tidal cycle of a morphodynamic run around the central sand wave. *Note the difference in the scales. For the Wave case almost all sediment is transported as bed load resulting in overlapping lines*

The inclusion of wind results in a tide-averaged ebb-directed bottom velocity. However, the largest velocities on the crest and steep slope are found during the flood and are flood-directed. Therefore the tide-averaged sediment transport is also flood-directed at the crest and steep slope. At the mild slope, the increased bottom velocities in the ebb direction result in large sediment transport rates in this direction, as can be seen in Figure 7b. The tide-averaged sediment transport has increased and is about 4 times as large compared to the Reference case. Both the sediment transport modes are in the same order, except at the mild slope where bed load is dominant.

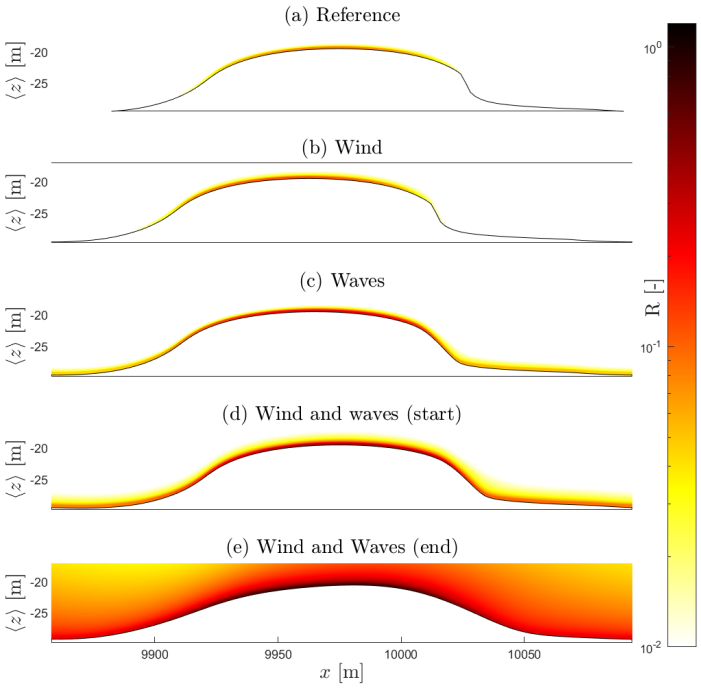

Figure 8: The sediment concentrations around the central sand wave during peak flow velocities of (a-d) the first flood and (e) during the last flood for the Wind and wave case.
Note that the bathymetries are already updating

Surface waves have a large effect on sediment transport rates due to increased turbulent kinetic energy. As a result, transport rates are increased by a factor of about 100 and are spatially distributed differently. The turbulence is increased, especially during ebb, which results in smaller horizontal bottom velocities and sediment transport is larger during ebb. Tide-averaged, the sediment transport is trough-directed and in the trough, the transport is directed towards the steep slope, as can be seen in Figure 7c. In the entire domain bed load transport is dominant, as can be seen in the same figure. The suspended sediment transport has largely increased compared to the reference case, however, transport during a flood is compensated during an ebb, resulting in limited tide-averaged suspended sediment transport.

In the Wind and wave case, the sediment transport processes are comparable to the Wave-case, although are increased over space and time due to wind-driven surface wave growth. The increased ebb-directed bottom flow results in larger sediment transport volumes. Due to the increase in surface wave heights, the suspended sediment concentrations increase over time as well. Figure 8e shows the sediment concentrations at the end of the simulation period. In the other cases, the suspended sediment concentrations are comparable during every tidal cycle.

5.2 Morphologic change

In the Reference case, the sand waves are stable in height and shape and are migrating in the flood direction by 1.4 m year^{-1}. This is expected as the equilibrium bed level is used. The migration is induced by tidal asymmetry, resulting in more sediment transport during flood compared to ebb. In general it can be seen that the largest morphological adaptation occurs during the first tidal cycle, information about the morphologic change over time can be seen in Appendix D.

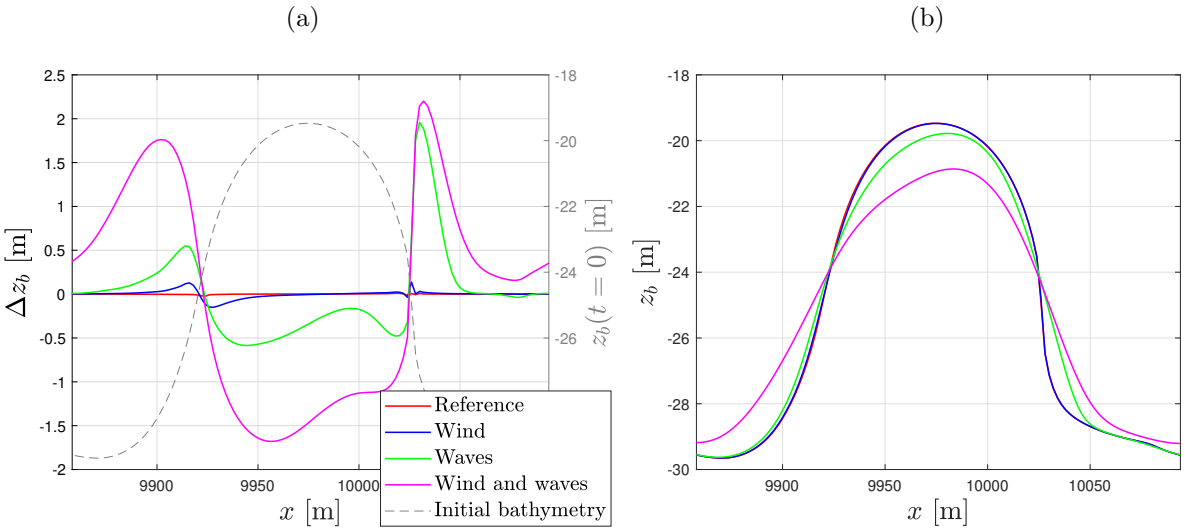

Figure 9: The morphological change for 5 tidal cycles (about 2.5 days) of the central sand wave, showing a) the spatially distributed erosion and sedimentation and b) the final bathymetries.

The inclusion of wind results in more ebb-directed bottom velocities and increased sediment transport rates mainly at the mild slope. The sediment transport results in a milder slope. The steep slope on the other hand does not show significant morphologic changes. Although the differences in the final bathymetries are hard to see (Fig 9a), the blue line in Figure 9b clearly shows that the top half of the sand wave is eroded, while the bottom half of the sand wave is accreted. Moreover, the sand wave is decreased in height by 0.01 m.

In the Wave-case, the trough-directed sediment transport results in milder slopes. The steep slope decreases in the first tidal cycle from 23 to about 14 °, after which both slopes gradually decrease. Over the entire sand wave area, sediments are transported to the steep slope, as can be seen in Figure 7c. Although, most of the sediments move in the ebb direction, the sand wave as a whole shows flood-directed migration, as sediments during wave action are transported from one sand wave to the downstream-located sand wave. This means that sand waves during storms are dependent on upstream-located sand waves for the sediment supply. Moreover, the sand wave is deformed as can be seen in Figure 9a, the profile has flattened, showing milder slopes, flatter crests, and less deep troughs. In total, the sand wave height has decreased by 0.35 m during 5 tidal cycles.

The combination of wind and surface waves results in the largest morphologic change, which mainly can be explained by the wind-driven growth of surface waves. The processes are comparable to the Wave case, although due to the additional return flow due to wind, the crest is more eroded, resulting in a milder mild slope and a total sand wave height decrease of 1.9 m.

Sand wave migration is hard to determine based on the short-term runs, combined with the large deformation of the sand wave, however, the top of the sand wave clearly shows migration in flood direction, as well for the Wave as the Wind and wave case.

5.3 Storm intensity

The impact of storms is dependent on the intensity of the storm, the previously discussed storms are once-in-a-100-year case storms and are thus rather seldom. Therefore it has been determined what the sensitivity of the storm intensity is for the Wind and wave case with smaller wind conditions, using equation 15. The subsequent wave conditions are determined based on the equations of Carter (1982) (eq. 13). For limited storms ($I < 0.4$), the sand wave dynamics are not affected significantly, as wind and wave conditions only have a limited impact on the bottom velocities. For larger velocities ($I > 0.4$), the hydrodynamics is affected by the storm conditions and increases for larger intensities. Especially during ebb, the velocities are increased, resulting in ebb-directed sediment transport. For moderate storms ($0.4 < I < 0.8$, sediment is mainly transported aon the sand wave itself, as velocities in the trough are not large enough to transport sediments. Therefore, this results in ebb-directed migration of the sand wave top, as can be seen in Figure 10c. For storm intensities of $I > 0.8$, the storm velocities are significantly larger compared to the return flow and are able to transport the sediments from the one sand wave to the other and thereby resulting in flood-directed sand wave migration. Moreover, the larger storm intensities, result in a decrease in sand wave heights (Figure 10b) and the sand wave slope decays up to about 10 to 15 °(Figure 10d). Interestingly, the sand wave slopes will not decay further independently of the storm intensity. The sediment transport, and suspended sediment concentrations however do still largely increase with storm intensity and instead of sand wave deformation, larger storms will mainly result in sediment transport and sand wave migration.

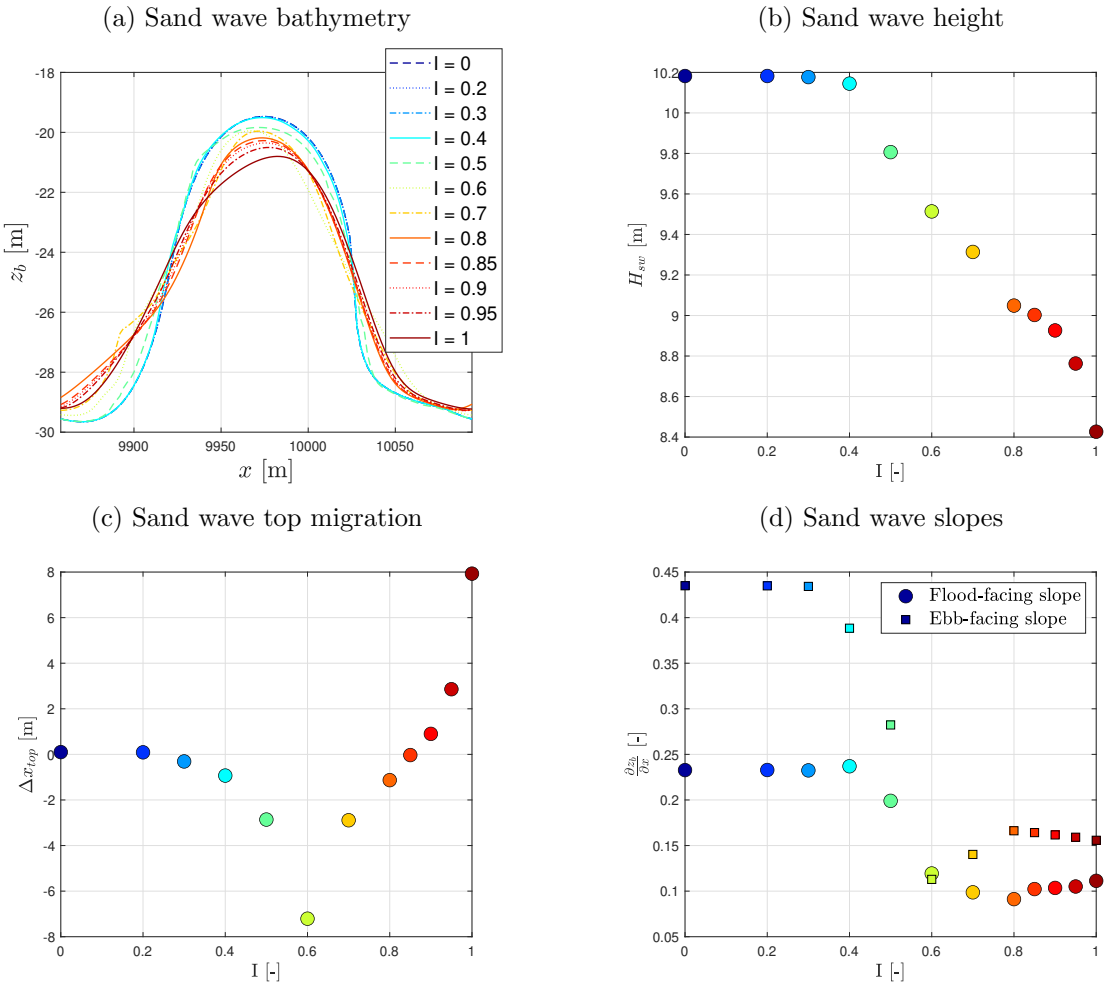

Figure 10: The effect of the storm intensity for the Wind and wave case for a run of 5 morphodynamical tidal cycles on the a) bathymetry, b) sand wave height, c) sand wave top migration, and d) sand wave slopes.

6 Discussion

This study gives insight into the hydro- and morphodynamic processes during storms. It shows the processes during wind and surface wave action and the resulting morphologic adaptions. The study is meant for a process-based analysis of the effects of storms on sand waves, in order to use this in a quantitative manner, more research is needed.

6.1 Comparison to other studies

Campmans et al. (2017), Bao et al. (2020), and Liang et al. (2022) conclude that the effect of storms results in decreased sand wave heights, and with that a flattening of the sand wave field, the same effect can also be seen in this model caused by wind and wave action. The sand wave decrease moreover is in the same order of magnitude compared to the measurements of Bao et al. (2020), 1.2 m. The measurements of Bao et al. (2020) and the study of Campmans et al. (2018b), suggest sand wave migration in the direction of the storm. The study of Liang et al. (2022) on the other hand, shows migration in the opposite direction. The results in Chapter 5 can explain the knowledge gap, as it is seen that the addition of waves results in anti-storm-directed migration of sediments, but storm-directed migration of the sand wave crests and troughs. In order to see how the sand waves fully recover after the storm, longer-term simulations are needed.

Campmans et al. (2017) shows an increase in sand wave wavelength under constant wind and wave forcing. In the short modeling period of 2.5 days, this can not be seen in our study. Regarding the short period, it can be concluded that short-term processes can have large effects on the sand wave dynamics, as is also seen in Campmans et al. (2017) and Bao et al. (2020). In this period, it is seen that large volumes of suspended sediment are transported. Liang et al. (2022) concluded that suspended sediment transport is dominant during storms. Although the transport volumes are dominant, the resultant tide-averaged morphologic change is limited.

This study differs from the other studies as it is the first model in which storm effects are measured over full-grown sand waves for a short period and therefore can be compared to measurement results. Moreover, the study includes a process-based analysis including surface elevation, however on the contrary, also a numeric setup in the surface level plays a role when modeling wave action and affecting the hydrodynamics.

6.2 Limitations in storm representation

The largest uncertainty in this study is that the addition of wind results in a mass drift which, due to numerical effects at the boundaries, results in a set-up and a pressure-driven return flow. This setup due to the wind is only found in (partially) closed basins (Međugorac et al., 2021), however for open basins the storm-driven setup is not seen. Instead, horizontal wind-driven circulation flows are detected during storms in the North Sea (Sündermann and Pohlmann, 2011). In the model, the once-in-a-100-year scenario with wind and surface waves results in a tide-averaged surface gradient of $5 \cdot 10^{-4}$°and is therefore limited. However, the influence of the return flow is large. About 20% of the negative tide-averaged wave profile (Figure 4) can be explained by wind affecting the top layers and therefore compressing the tidal flow towards the bottom layers, resulting in extra large velocities. The remaining 80% of the ebb-directed bottom flow is caused by the return flow, as is tested by comparison to a wind-only run (so without tidal forcing). In reality, the dominant ebb-directed flow will therefore be smaller. However, it is expected that the ebb-directed sediment transport will remain dominant as turbulence levels during ebb are larger and ebb-directed sediment transport is largest as well in the Wave-case. The hydrodynamic bottom conditions in the Wave case and the Wind and wave case are namely comparable when comparing equal actual surface wave conditions.

In the model, the storm effects are modeled as constant wind and surface wave action acting on the sand wave system. Hereby extreme once-in-a-100-year conditions, acting from flood direction are used. In reality, there is always a build-up in wind and wave conditions, that already affect

the bathymetry before the extreme conditions are present. Those increase the suspended sediment concentrations and are expected to enhance sediment transport. Moreover, at the end of the storm, a gradual decrease in storm conditions is present, which results in the settling of sediments. The hydrodynamic conditions during the settlement might influence the morphologic change. Moreover, storms, in general, originate from the West, resulting in an offset between the storm and the sand wave of about 45°and thereby decreasing the effect of the storm, as Campmans et al. (2018b) found that storms parallel to the tidal direction have a larger morphodynamic influence compared to oblique storm directions. On the other hand, the most extreme storms originate from the North-side, as that direction has the largest fetch, and therefore has an offset of about 45°with respect to the ebb-directed flow.

Smaller bed patterns such as ripples are dynamic and enhance morphodynamic changes (Brakenhoff et al., 2020). During large storms, these bed forms can be flatted or even be washed out (Passchier and Kleinhans, 2005), affecting the bottom roughness abruptly (Hay, 2011). In the model, smaller bed forms are including via the bottom roughness, with is modelled as a constant Chézy value of 75 $m^{\frac{1}{2}}s^{-1}$, representing a smooth bed. A spatially and temporally varying Chézy coefficient would improve the model. Areas in which ripples are not totally flatted during storms (i.e. the troughs) then have more sediment transport (Rijn et al., 2003; Brakenhoff et al., 2020).

In the model, the sediment transport equations of van Rijn (1993) are used to model erosion and sedimentation based on shear stresses and mass settling. Hereby it is assumed that sediments are distributed equally over the domain. However, in reality, the particles are sorted over the sand wave, resulting in larger sediment particles at the crest and smaller sediment particles in the troughs (Damveld et al., 2020). Therefore erosion is overestimated at the crests and underestimated at the troughs. Moreover, according to Wang et al. (2018), instead of bed and suspended sediment transport, storms can also result in storm-induced sub-aqueous land sliding, resulting in large instantaneous sand wave deformation, which is not included in the model.

6.3 Numerical limitations

From a numerical point of view, the step size in time and the grid size in space oif Delft3D-Flow are adequately defined to model hydro- and morphodynamic effects, as the convergence in time and space is verified. However, for the Delft3D-Wave module, this is not tested and the wave field neither is constant in space, showing large variations at the larger grid sizes nor in time. For the Wave-case, the surface waves moreover decrease in height over space, due to the lack of wind-induced growth. In the wind and wave case, the surface waves increase in height over time due to the constant wind growth acting on the system. In the area of interest, the wave heights are relatively constant (a decline of about 2% of the surface wave height over 1.2 km) but do not match the boundary conditions. Therefore, the morphologic results should be judged based on the conditions in the model (see Table 2) instead of the boundary conditions.

Moreover, the resolution of the horizontal grid in the Flow module is not large enough to accurately define the velocity field on the steep side of every sand wave. Delft3D with a σ-grid assumes small aspect ratios, such that the vertical momentum equation can be reduced to the hydrostatic pressure relation. However, this can result in significant density gradient errors in areas with steep bottom topography (Stelling and Van Kester, 1994). In the equilibrium bathymetry, a 3.0 m height difference is covered in one step ($\Delta x = 2$ m) at the steepest location. This can result in unrealistic velocities and large local sedimentation volumes. Moreover, the α_s, as is defined in Appendix A, will become negative for slopes larger than $\frac{\partial z}{\partial s} = 0.7$ [-]. Therefore no bed load sediment transport in the ebb direction at the steep side of the sand wave is allowed. In total, the hydro- and morphodynamics at the steepest part of the sand wave can not be fully trusted, resulting in locally overestimated netto flood-directed transport. It has been tested to locally refine the grid, although this has resulted in even steeper local rates due to smaller steps.

Last but not least, the suspended sediment concentrations in Delft3D largely increase when the tidal velocity approaches 0 m s^{-1}. This is caused by the effect of the Stokes drift on the bed shear

stress (as can be seen in equation 7) that becomes dominant compared to $\vec{u}$ and is a numerical error. Although suspended sediment concentrations largely increase, the resultant sediment transport is limited as the velocities are small, and therefore sediment is not replaced.

6.4 Future research

In this study, single storm events are modeled on an equilibrium bathymetry originating from pure tidal forces. In reality, both conditions interplay with each other. In the reference case, wind and wave conditions for fair weather should be added to find the long-term fair weather equilibrium. Moreover, after storms fair weather conditions should be modeled to see what effects the distortion from storm conditions has on the longer term and how suspended sediment concentrations settle. The short-term storm changes can namely be a trigger for different modes to establish, through deformation, or for large migration effects. In total, it is interesting whether sand waves are able to grow to their tidal equilibrium height or whether the sand waves are hardly able to establish before the next storm arises.

The model is made in 2DV, meaning that effects in the third dimension are removed. Wind and waves are also only analyzed in flood direction. In the study of (Campmans, 2018a) it is found that storms parallel to the tidal direction have a larger influence compared to oblique storm directions. The same study however also shows that wind perpendicular to the tidal flow however increases sand wave heights. Future research into storms perpendicular to the tidal flow is therefore of interest.

7 Conclusion

The Delft3D model of van Gerwen et al. (2018) has been adjusted to include the effects of wind and surface waves on sand wave dynamics. Therefore 6 processes are added to the system; (i) wind-driven shear stress on the water surface, (ii) wind-driven surface wave growth, (iii) wind and wave-induced turbulence, (iv) surface wave-induced bed shear stress, (v) surface-wave induced mass drift and (vi) its shear stress due to streaming. Moreover, asymmetric tidal conditions (incl. surface elevation) are used to create a full-grown sand wave field consisting of several sand waves. In this model, the effects of wind, surface waves, and the combination of them are tested for 5 tidal cycles based on extreme once-in-a-100-year storm conditions.

The addition of wind results in increased ebb-directed bottom velocities, partly caused by the numerical set up cased by a wind-driven mass drift. At the mild slope, increased ebb-directed bottom velocities, erode sediments and transport them downslope, resulting in a milder slope. Surface waves create extra turbulent kinetic energy and moreover show dominant wave-directed flow. The bottom velocity field becomes trough-directed and sediment transport increases resulting in a flatter sand wave. In the trough, sediments are transported anti-wind-directed and settle at the steep slope of the sand wave, resulting in storm-directed migrating sand waves. The combination of wind and surface waves mainly increases surface wave growth and therefore results in larger turbulence and morphologic adaptations. Herein, the effect of wind shear stress on the top surface is marginal compared to the effect of surface waves.

Moreover, there is clear deformation of the sand waves, the sand waves are flattened and slopes are reduced by the interaction of surface waves, which results in more symmetric sand waves. Migration rates of the entire sand wave are hard to determine based on 5 tidal cycles full of morphological development and deformation. However, based on the displacement of the tops, it can be seen that during limited storms, the migration is in the ebb-direction, while during extreme storms, flood-directed migration of sand waves is observed. These morphological effects of the once-in-a-100-year storm scenarios result in sand wave flattening that will take decades to recover based on tidal flows only. This means that the dynamic equilibrium of sand waves is largely influenced by storms. This means that the influence of storms should be taken into consideration while determining the equilibrium sand wave profiles and the possible morphologic variations.

Bibliography

Babanin, A. (2006). "On a wave-induced turbulence and a wave-mixed upper ocean layer". In: *Geophysical Research Letters* 33.20. DOI: https://doi.org/10.1029/2006GL027308.

Bao, J., F. Cai, F. Shi, C. Wu, Y. Zheng, H. Lu, and L. Sun (2020). "Morphodynamic response of sand waves in the Taiwan Shoal to a passing tropical storm". In: *Marine Geology* 426, p. 106196. DOI: https://doi.org/10.1016/j.margeo.2020.106196. URL: https://www.sciencedirect.com/science/article/pii/S0025322720300840.

Besio, G., P. Blondeaux, and G. Vittori (2006). "On the formation of sand waves and sand banks". In: *Journal of Fluid Mechanics* 557, pp. 1–27. DOI: https://doi.org/10.1017/S0022112006009256.

Besio, G., P. Blondeaux, M. Brocchini, and G. Vittori (2003). "Migrating sand waves". In: *Ocean Dynamics* 53.3, pp. 232–238. DOI: 10.1007/s10236-003-0043-x.

Borsje, B. W., P. C. Roos, W. Kranenburg, and S. J. M. H. Hulscher (2013). "Modeling tidal sand wave formation in a numerical shallow water model: The role of turbulence formulation". In: *Continental shelf research* 60, pp. 17–27. DOI: https://doi.org/10.1016/j.csr.2013.04.023.

Brakenhoff, L., R. Schrijvershof, J. van der Werf, B. Grasmeijer, G. Ruessink, and M. van der Vegt (2020). "From ripples to large-scale sand transport: The effects of bedform-related roughness on hydrodynamics and sediment transport patterns in delft3d". In: *Journal of marine science and engineering* 8.11, p. 892. DOI: https://doi.org/10.3390/jmse8110892.

Bremer, T. S. van den and Ø. Breivik (2018). "Stokes drift". In: *Philosophical Transactions of the Royal Society A: Mathematical, Physical and Engineering Sciences* 376.2111, p. 20170104. DOI: 10.1098/rsta.2017.0104.

Caires, S., J. Groeneweg, and A. Sterl (2006). "Changes in the North Sea extreme waves". In: *Preprints of 9th international workshop on wave hindcasting and forecasting*.

Campmans, G., P. Roos, H. de Vriend, and S. J. M. H. Hulscher (2017). "Modeling the influence of storms on sand wave formation: A linear stability approach". In: *Continental Shelf Research* 137, pp. 103–116. DOI: https://doi.org/10.1016/j.csr.2017.02.002.

Campmans, G. H. P. (2018a). "Modeling storm effects on sand wave dynamics". In: *University of Twente PhD Thesis*. DOI: https://doi.org/10.3990/1.9789036546003.

Campmans, G., P. Roos, H. De Vriend, and S. J. M. H. Hulscher (2018b). "The influence of storms on sand wave evolution: a nonlinear idealized modeling approach". In: *Journal of Geophysical Research: Earth Surface* 123.9, pp. 2070–2086. DOI: https://doi.org/10.1029/2018JF004616.

Carter, D. (1982). "Prediction of wave height and period for a constant wind velocity using the JONSWAP results". In: *Ocean Engineering* 9.1, pp. 17–33. DOI: https://doi.org/10.1016/0029-8018(82)90042-7.

Damen, J. M., T. A. G. P. van Dijk, and S. J. M. H. Hulscher (2018). "Spatially varying environmental properties controlling observed sand wave morphology". In: *Journal of Geophysical Research: Earth Surface* 123.2, pp. 262–280. DOI: https://doi.org/10.1002/2017JF004322.

Damveld, J., B. Borsje, P. Roos, and S. J. M. H. Hulscher (2020). "Horizontal and vertical sediment sorting in tidal sand waves: modeling the finite-amplitude stage". In: *Journal of Geophysical Research: Earth Surface* 125.10, e2019JF005430. DOI: https://doi.org/10.1029/2019JF005430.

Deltares (2023a). *Delft3D Flow Manual Hydro-Morphodynamics*. Version: 4.05. Revision: 77288. Deltares. Delft, the Netherlands.

— (2023b). *Delft3D Wave Manual Hydro-Morphodynamics*. Version: 4.05. Revision: 76992. Deltares. Delft, the Netherlands.

Dijk, T. A. van and M. G. Kleinhans (2005). "Processes controlling the dynamics of compound sand waves in the North Sea, Netherlands". In: *Journal of Geophysical Research: Earth Surface* 110.F4. DOI: https://doi.org/10.1029/2004JF000173.

Fenster, M., D. FitzGerald, W. Bohlen, R. Lewis, and C. Baldwin (1990). "Stability of giant sand waves in eastern Long Island Sound, U.S.A". In: *Marine Geology* 91, pp. 207–225. DOI: https://doi.org/10.1016/0025-3227(90)90037-K.

Gargett, A. E. and D. K. Savidge (2020). "Winds, waves, and turbulence on a shallow continental shelf during passage of a tropical storm". In: *Journal of Physical Oceanography* 50.5, pp. 1341–1364. DOI: https://doi.org/10.1175/JPO-D-20-0024.1.

Gerwen, W. van, B. W. Borsje, J. H. Damveld, and S. J. M. H. Hulscher (2018). "Modelling the effect of suspended load transport and tidal asymmetry on the equilibrium tidal sand wave height". In: *Coastal Engineering* 136, pp. 56–64. DOI: https://doi.org/10.1016/j.coastaleng.2018.01.006.

Gräwe, U., H. Burchard, M. Müller, and H. M. Schuttelaars (2014). "Seasonal variability in M2 and M4 tidal constituents and its implications for the coastal residual sediment transport". In: *Geophysical Research Letters* 41.15, pp. 5563–5570.

Hasselmann, S., K. Hasselmann, J. Allender, and T. Barnet (1985). "Computations and parameterizations of the nonlinear energy transfer in a gravity wave spectrum. Part II: Parameterizations of the nonlinear transfer for application in wave models." In: *Journal of Physical Oceanography*. DOI: https://doi.org/10.1175/1520-0485(1985)015⟨1378:CAPOTN⟩2.0.CO;2.

Hay, A. E. (2011). "Geometric bed roughness and the bed state storm cycle". In: *Journal of Geophysical Research: Oceans* 116.C4. DOI: https://doi.org/10.1029/2010JC006687.

Hoood, R. (2017). *Landscape cross section with Blue Sky and sun background*. URL: https://www.istockphoto.com/nl/foto/dwarsdoorsnede-van-de-grond-en-zee-gm656238876-119447015.

Hulscher, S. J. M. H. (1996). "Tidal-induced large-scale regular bed form patterns in a three-dimensional shallow water model". In: *Journal of Geophysical Research: Oceans* 101.C9, pp. 20727–20744. DOI: https://doi.org/10.1029/96JC01662.

Hulscher, S. J. M. H., H. E. de Swart, and H. J. de Vriend (1993). "The generation of offshore tidal sand banks and sand waves". In: *Continental Shelf Research* 13.11, pp. 1183–1204. DOI: https://doi.org/10.1016/0278-4343(93)90048-3.

Jänicke, L., A. Ebener, S. Dangendorf, A. Arns, M. Schindelegger, S. Niehüser, I. D. Haigh, P. Woodworth, and J. Jensen (2021). "Assessment of tidal range changes in the North Sea from 1958 to 2014". In: *Journal of Geophysical Research: Oceans* 126.1, e2020JC016456. DOI: https://doi.org/10.1029/2020JC016456.

Knaapen, M. (2005). "Sandwave migration predictor based on shape information". In: *Journal of Geophysical Research: Earth Surface* 110.F4. DOI: https://doi.org/10.1029/2004JF000195.

Komen, G., S. Hasselmann, and K. Hasselmann (1984). "On the existence of a fully developed wind-sea spectrum". In: *Journal of physical oceanography* 14.8, pp. 1271–1285. DOI: https://doi.org/10.1175/1520-0485(1984)014⟨1271:OTEOAF⟩2.0.CO;2.

Kumar, P., S. E. Debele, J. Sahani, N. Rawat, B. Marti-Cardona, S. M. Alfieri, B. Basu, A. S. Basu, P. Bowyer, N. Charizopoulos, et al. (2021). "Nature-based solutions efficiency evaluation against natural hazards: Modelling methods, advantages and limitations". In: *Science of the Total Environment* 784, p. 147058. DOI: https://doi.org/10.1016/j.scitotenv.2021.147058.

Lee, J. and J. Monty (2020). "On the interaction between wind stress and waves: Wave growth and statistical properties of large waves". In: *Journal of Physical Oceanography* 50.2, pp. 383–397. DOI: https://doi.org/10.1175/JPO-D-19-0112.1.

Liang, B., Z. Wang, B. Xie, G. Wu, Z. Yan, and B. Borsje (2022). "The role of idealized storms on the initial stages in sand wave formation: A numerical modeling study". In: *Ocean Engineering* 262, p. 112203. DOI: https://doi.org/10.1016/j.oceaneng.2022.112203.

Makin, V. K. (2005). "A note on the drag of the sea surface at hurricane winds". In: *Boundary-layer meteorology* 115, pp. 169–176. DOI: https://doi.org/10.1007/s10546-004-3647-x.

Međugorac, I., M. Pasarić, and I. Güttler (2021). "Will the wind associated with the Adriatic storm surges change in future climate?" In: *Theoretical and Applied Climatology* 143.1-2, pp. 1–18. DOI: https://doi.org/10.1007/s00704-020-03379-x.

Naqshband, S., J. S. Ribberink, D. Hurther, and S. J. M. H. Hulscher (2014). "Bed load and suspended load contributions to migrating sand dunes in equilibrium". In: *Journal of Geophysical Research: Earth Surface* 119.5, pp. 1043–1063. DOI: https://doi.org/10.1002/2013JF003043.

Overes, P. (2021). "Modeling Sand Wave Field Dynamics in the North Sea using Delft3D Flexible Mesh". MA thesis. the Netherlands: TU Delft.

Passchier, S. and M. Kleinhans (2005). "Observations of sand waves, megaripples, and hummocks in the Dutch coastal area and their relation to currents and combined flow conditions". In: *Journal of Geophysical Research: Earth Surface* 110.F4. DOI: https://doi.org/10.1029/2004JF000215.

Pedersen, M. W., D. Righton, U. H. Thygesen, K. H. Andersen, and H. Madsen (2008). "Geolocation of North Sea cod (Gadus morhua) using hidden Markov models and behavioural switching". In: *Canadian Journal of Fisheries and Aquatic Sciences* 65.11, pp. 2367–2377. DOI: https://doi.org/10.1139/F08-144.

Reynaud, J.-Y. and R. W. Dalrymple (2012). "Shallow-marine tidal deposits". In: *Principles of tidal sedimentology*, pp. 335–369. DOI: https://doi.org/10.1007/978-94-007-0123-6_13.

Rijn, L. C. van (1993). *Principles of sediment transport in rivers, estuaries and coastal seas*.

Rijn, L. C. van, D. J. Walstra, B. Grasmeijer, J. Sutherland, S. Pan, and J. Sierra (2003). "The predictability of cross-shore bed evolution of sandy beaches at the time scale of storms and seasons using process-based profile models". In: *Coastal Engineering* 47.3, pp. 295–327. DOI: https://doi.org/10.1016/S0378-3839(02)00120-5.

Stelling, G. S. and J. A. T. M. Van Kester (1994). "On the approximation of horizontal gradients in sigma co-ordinates for bathymetry with steep bottom slopes". In: *International Journal for Numerical Methods in Fluids* 18.10, pp. 915–935. DOI: https://doi.org/10.1002/fld.1650181003.

Sterl, A., A. M. Bakker, H. W. van den Brink, R. Haarsma, A. Stepek, I. L. Wijnant, and R. C. de Winter (2015). "Large-scale winds in the southern North Sea region: the wind part of the KNMI'14 climate change scenarios". In: *Environmental Research Letters* 10.3, p. 035004. DOI: https://doi.org/10.1175/JCLI-3312.1.

Sumner, D. (2023). *Sediments and Strata — Chapter 9.5: Sediment Transport*. LibreTexts, University of California.

Sündermann, J. and T. Pohlmann (2011). "A brief analysis of North Sea physics". In: *Oceanologia* 53, pp. 663–689. DOI: 10.5697/oc.53-3.663.

Tanaka, H. et al. (2009). "Effect of bed roughness on turbulent boundary layer and net sediment transport under asymmetric waves". In: *Coastal Engineering* 56.9, pp. 960–969. DOI: https://doi.org/10.1016/j.coastaleng.2009.06.005.

Tonnon, P., L. Van Rijn, and D. Walstra (2007). "The morphodynamic modelling of tidal sand waves on the shoreface". In: *Coastal Engineering* 54.4, pp. 279–296. DOI: https://doi.org/10.1016/j.coastaleng.2006.08.005.

Vrees, L. de (2021). "Adaptive marine spatial planning in the Netherlands sector of the North Sea". In: *Marine Policy* 132, p. 103418. DOI: https://doi.org/10.1016/j.marpol.2019.01.007. URL: https://www.sciencedirect.com/science/article/pii/S0308597X18304597.

Wang, Z., Y. Jia, X. Liu, D. Wang, H. Shan, L. Guo, and W. Wei (2018). "In situ observation of storm-wave-induced seabed deformation with a submarine landslide monitoring system". In: *Bulletin of Engineering Geology and the Environment* 77.3, pp. 1091–1102. DOI: https://doi.org/10.1007/s10064-017-1130-4.

Wang, Z., B. Liang, G. Wu, and B. Borsje (2019). "Modeling the formation and migration of sand waves: The role of tidal forcing, sediment size and bed slope effects". In: *Continental Shelf Research* 190, p. 103986. DOI: https://doi.org/10.1016/j.csr.2019.103986.

Weijgaert, R. van de (2014). *Lecture Notes Chapter 7 Shocks*. URL: https://www.astro.rug.nl/~weygaert/tim1publication/astrohydro2014/achterberg.ngsa.shockwaves.pdf.

Werf, J. J. van der, R. A. Schrijvershof, L. B. Brakenhoff, and B. T. Grasmeijer (2022). "Observations of near-bed orbital velocities and small-scale bedforms on the Dutch lower shoreface". In: *Ocean & coastal management* 218, p. 106012. DOI: https://doi.org/10.1016/j.ocecoaman.2021.106012.

A Explanation transport equations

As can be seen in Chapter 2, sediment transport is described by the sediment transport equations of Rijn (1993), which are based on a formula for bed load transport (eq. 10 as well as a formula for suspended load transport 11. In equation 10, ρ_s is the sediment density [kg m^{-3}], w_s is the particle settling velocity in a mixture [m s^{-1}] and D_{50} is the median sediment diameter [m]. Furthermore, the bed load transport is dependent on the sediment mobility due to waves (M [-]) and excess sediment mobility number (M_e [-]), which are defined as

$$M = \frac{v_{eff}^2}{(s-1)gD_{50}} \tag{16}$$

$$M_e = \frac{(v_{eff} - v_{cr})^2}{(s-1)gD_{50}} \tag{17}$$

in which, v_{eff} is the effective velocity, which is the combination of the near bottom velocity magnitude (v_R) and the near-bed orbital velocity in the onshore direction (U_{on}), along $v_{eff} = \sqrt{v_R^2 + U_{on}^2}$. Moreover, v_{cr} is the critical depth-averaged velocity for motion initiation [m s^{-1}], g is the gravitational acceleration $g = 9.81$m s^{-2}, D_{50} is the median sediment diameter [m] and s is the relative sediment density ($s = \frac{\rho_s}{\rho_w}[-]$) or sediment ($\rho_s$) compared to water ($\rho_w$).

The bed load transport moreover, is affected by the bed level gradients using the α_s, which is defined as,

$$S_b' = \alpha_s S'' \tag{18}$$

hereby, the α_s is calculated using;

$$\alpha_s = 1 + \alpha_{bs}\left(\frac{tan(\phi)}{cos\left(tan^{-1}\left(\frac{\partial z}{\partial s}\right)\right)\left(tan(\phi) + \frac{\partial z}{\partial s}\right)} - 1\right) \tag{19}$$

where ϕ is the internal angle of friction of bed material [°] and $\frac{\partial z}{\partial s}$ is the bed level gradient [-]. For using a default $\phi = 30°$ it is found that for bed level gradients larger than 0.7, no sediment is able to be transported upwards.

The direction of bed load transport is determined by comparing the bottom velocity magnitude (v_R) and the wave-induced orbital bottom velocities (U_{on}) to the critical depth-averaged velocity for motion initiation (v_{cr}), using $r = \frac{(U_{on}-v_{cr})^3}{(v_R-v_{cr})^3}$. If $r < 0.01$, the bed load direction is determined by the bottom velocity magnitude, but if $r > 100$, the sediment transport is in the direction of wave propagation, and thus opposed to the bottom flow direction. In all other cases, the direction is determined by a combination of both.

The suspended sediment transport is computed using eq. 11, where f_{SUSW} is a user-defined tuning parameter ($f_{SUSW} = 1$ [-]) and γ is the phase lag coefficient ($\gamma = 0.2$ [-]). U_A is the velocity asymmetry, defined as $U_A = \frac{U_{on}^4 - U_{off}^4}{U_{on}^3 + U_{off}^3}$, and thus indicates the asymmetry between the bottom orbital velocities (U_{on} and U_{off} [m s^{-1}]), where U_on is in direction of the wave propagation and U_off is opposed to the wave propagation direction. The last factor is the suspended sediment load (L_T [kg m^{-2}]), which is defined as $L_T = 0.007\rho_s D_{50} M_e$.

B Model formation

B.1 Tidal forcing

Tidal forcing in the model is implemented using the Riemann invariant. The Riemann invariant can be used as a boundary condition, in which waves are able to propagate through a flow. In fact, it combines the local velocity with the general flow (Weijgaert, 2014). This is called a weakly reflective boundary and results in waves being able to propagate out of the domain. Using velocity or surface elevation boundaries, on the other hand, results in the reflection of (tidal) waves at the boundaries. The Riemann invariant is a combination of the flow and surface elevation, using the shallow wave assumption in Delft3D, the Riemann invariant (R [ms^{-1}]), is defined as,

$$R = U \pm 2\sqrt{gH} = U \pm \left(2\sqrt{gd} + \zeta\sqrt{\frac{g}{d}}\right), \tag{20}$$

where U is the velocity [ms^{-1}], g is the gravitational acceleration [ms^{-1}] and H is the total water depth [m], ζ is the surface elevation [m] and d is the depth to the mean water surface. Hereby, the second expression is the linearized version in which the $2\sqrt{gd}$-term is constant and will be calculated by Delft3D itself. Therefore the manual input ($f(t)$) of the flow at the boundary is defined by

$$f(t) = U \pm \zeta\sqrt{\frac{g}{d}}. \tag{21}$$

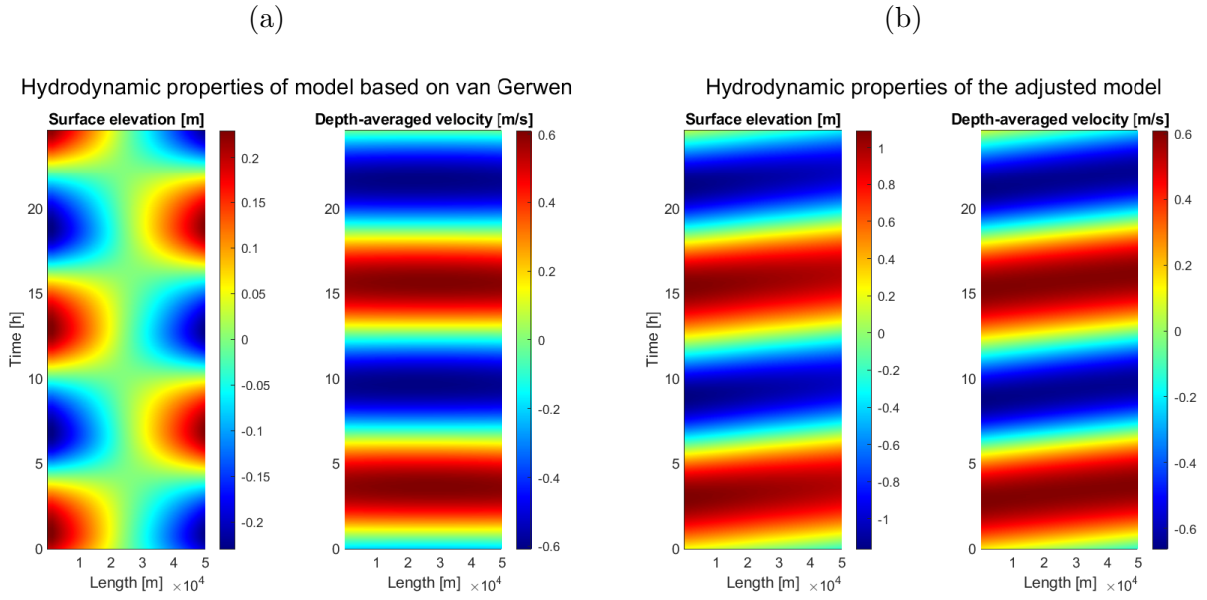

Figure B.1: Hydrodynamical properties of (a) a system with equal in- and outflow boundary conditions as in Gerwen et al. (2018) and (b) forced tidal inflow with undisturbed outflow (R = 0 m/s) both on a 50 km long flat domain.
Note that the surface elevation in (a) is much smaller compared to (b).

There are two open boundaries, parallel to the sand waves' crests, on which the tidal forcing is constrained using Riemann invariants. In Borsje et al. (2013) and Gerwen et al. (2018) the tidal forcing is applied on both boundaries resulting in an in-phase velocity field with no surface elevation in the center, as can be seen in the left pictures of Figure B.1a. Contradicting to this, the tidal forcing in this model is only applied on one boundary. On the other boundary, a Riemann invariant of 0 m/s ensures an almost undisturbed outflow of the tide. This results in a spatially and temporally propagating tidal wave, where the wave propagation is determined by the model characteristics such as the bathymetry, resulting in a shift in periodicity between the in- and outflow water heights and velocity, as can be seen in Figure B.1b.

B.2 Equilibrium bathymetry

The equilibrium bathymetry is determined by a FGM analysis. Based on an initial sand wave field of 5 waves of 0.1 m high, growth rates are determined using a Morphological acceleration factor of 10. The sand wave length of 232 m shows the largest growth rate which is 0.045 year^{-1}. This sand wave length and growth rate are comparable to other studies (Damveld et al., 2020).

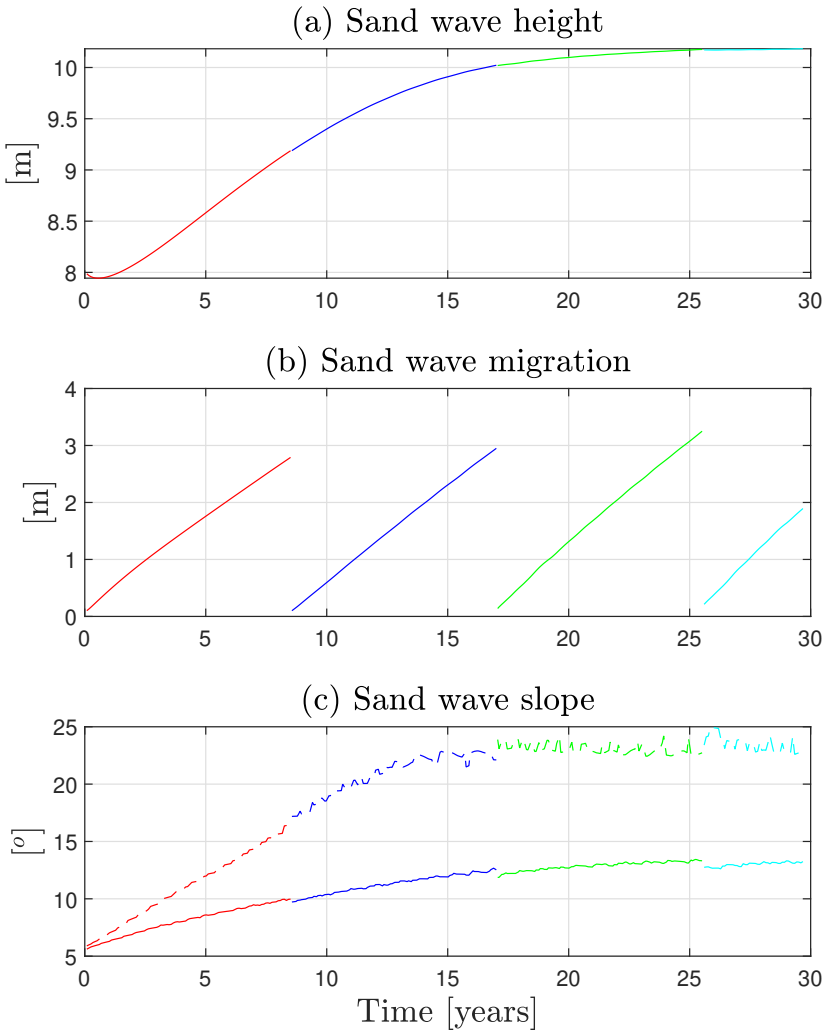

Figure B.2: Sand wave formation in 4 subsequent simulations exposed to asymmetric tidal forcing, starting with 8 m large symmetrical sand waves based on the FGM-mode

The bathymetry is determined, starting from 8-meter large symmetrical sand waves. When exposed to tidal forcing, they are grown up to 10.2 m. This process can be seen in Figure B.2, and consists of 4 different runs. In these runs, the sand waves are migrated in flood direction, over the grid. Therefore, at the end of every run, the sand wave field is spline interpolated on the grid and thus shifted in the ebb direction. The migration rate decreases over time, however, in reality, asymmetric sand waves migrate faster compared to symmetric sand waves. This can be explained by the fact that sand waves mainly deform, resulting in sand wave migration.

In Figure B.2 it can be seen that the migratoin at the start of the run is always a bit larger than expected based on previous runs, this is caused by the interpolation, which makes that some points might be shifted as a result. Moreover, it can be seen that there is a certain error margin for the slope.

C Model outcomes

In Table 2 several output values of the Delft3D-Flow and Delft3D-Wave modules are represented per case.

Table 2: Data per run

Case	I	$H_s w$	λ	ϕ_{mild}	ϕ_{steep}	H_s	T_s	Δz_0
	-	m	m	°	°	m	s	m
Reference	0.0	10.2	235.4	13.1	23.5	0.0	0.0	0.0
Wind	1.0	10.2	235.5	12.6	23.5	0.0	0.0	0.19
Waves	1.0	9.9	235.6	11.0	12.5	6.3	8.6	0.10
Wind and waves	1.0	8.7	236.5	7.1	9.1	9.1	8.2	0.17
Wind and Waves	0.2	10.2	235.4	13.1	23.5	1.4	3.7	0.00
Wind and Waves	0.3	10.2	235.4	13.1	23.5	3.5	5.3	-0.04
Wind and Waves	0.4	10.1	235.5	13.1	21.2	3.8	5.4	-0.02
Wind and Waves	0.5	9.8	235.7	11.3	15.8	5.6	6.3	-0.09
Wind and Waves	0.6	9.5	235.6	6.8	6.4	7.2	6.9	-0.23
Wind and Waves	0.7	9.3	234.6	5.6	8.0	7.6	7.1	-0.17
Wind and Waves	0.8	9.0	240.5	5.2	9.4	8.4	7.6	0.02
Wind and Waves	0.9	9.0	240.1	5.8	9.3	8.6	7.7	0.06
Wind and Waves	0.9	8.9	239.3	5.9	9.2	8.7	7.8	0.09
Wind and Waves	1.0	8.8	238.1	6.0	9.0	8.8	7.9	0.10

D Morphologic changes over time

The morphologic change is not constant over time. Actually, most of the morphological deformation occurs during the first tidal period, as can be seen in Figure D.1d. Despite the fact that the surface waves increase in height during the Wind and wave case, the deformation mainly occurs during the first tidal cycle. On the other hand, the sand wave height decrease, and top displacement continue over time, as can be seen in the Wave case. For the Wind and wave case, this even increases due to the surface wave increase over time. It can thus be concluded that the deformation, with rather large local height changes, occurs in a very limited time, while sand wave decrease and top displacement are more gradual processes.

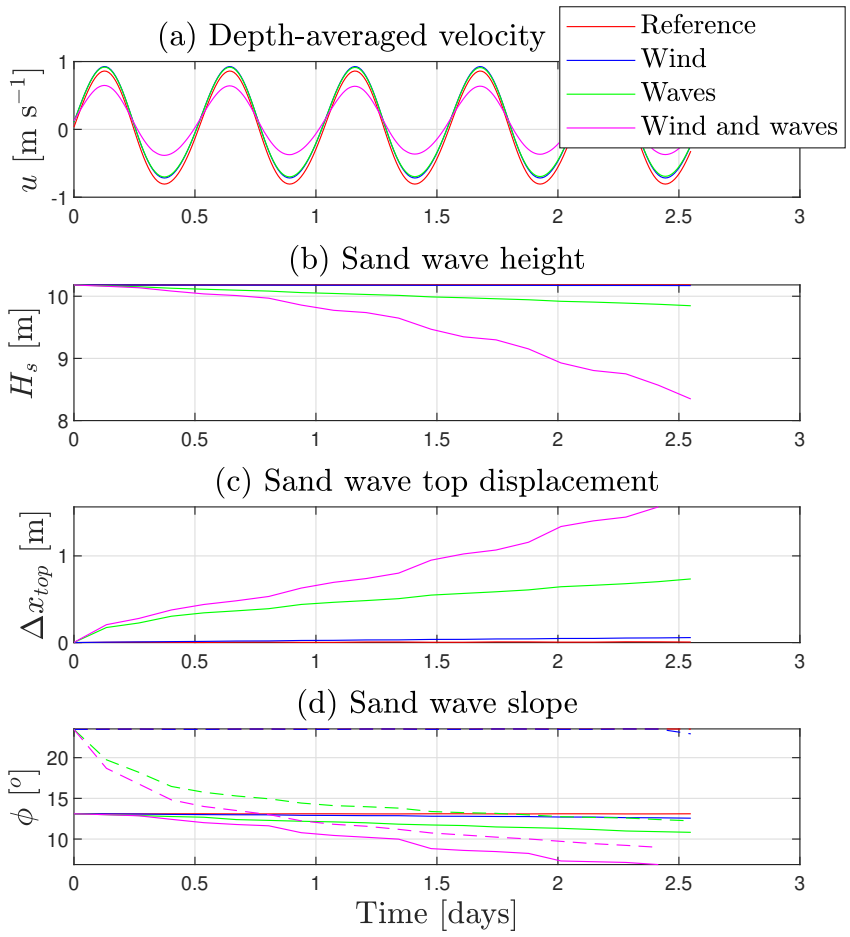

Figure D.1: The evolution of the sand wave characteristics for 5 tidal cycles based on morphodynamical runs for all cases. In (d) the dashed line shows the steep slope and the solid line the mild slope